Computational modeling of neurovascular coupling at the gliovascular interface

Dupeuble Florian[1]*, Berry Hugues[1], Denizot Audrey[1]*

1 AIstroSight, Inria, Hospices Civils de Lyon, Universite Claude Bernard Lyon 1, F-69603 Villeurbanne, France

* florian.dupeuble@inria.fr ; audrey.denizot@inria.fr

Abstract

A growing number of studies indicate the possible involvement of astrocytes in triggering or modulating neurovascular coupling (NVC), i.e. the local dilation of blood vessels in the brain in response to neuronal activity. Astrocytes possess specialized subcellular compartments, named endfeet, that surround arterioles and capillaries, ideally positioned to mediate NVC. Various vasodilators have been shown to contribute to NVC, such as epoxyeicosatrienoic acid (EET), nitric oxide (NO), or prostaglandin E2 (PGE2), but the precise mechanisms underlying NVC and their variability remain to be fully elucidated. In particular, the involvement of astrocytes in this process is controversial. Recent translatome and proteomics data reveal that astrocytes and in particular endfeet are enriched in the proteins of the PGE2 pathway. However, how the latter could contribute to NVC remains to be characterized. Here, we develop a computational model of astrocyte-mediated NVC that recapitulates these findings and describes Ca^{2+} and PGE2 signaling in astrocytes, NO release by neurons, and arteriole diameter dynamics using ordinary differential equations. The model successfully reproduces the dynamics of arteriole diameter change during hyperemia from *in vivo* neocortical recordings in awake mice. Our simulations suggest that the astrocyte PGE2 pathway could be responsible for the late response of NVC at the arteriolar level. We further observe that PIP2-derived diacylglycerol plays a major role in driving arteriole diameter dynamics in our model, while phosphatidic acid-derived diacylglycerol, which is calcium-dependent, mainly acts as an amplifier of this response. Finally, a spatial implementation of the model using a simplified astrocyte geometry suggests that NVC is more efficient when synaptic stimulation occurs at the endfoot level rather than at other astrocytic compartments. Overall, this computational study suggests a partial role for astrocyte-mediated PGE2 release in NVC and points to astrocyte perivascular processes as sub-compartments that are ideally positioned and equipped to mediate NVC.

Author summary

In the brain, the local blood flow is regulated to meet neuronal energy demand by modulating the dilation of neighboring blood vessels. The mechanisms driving this process, known as neurovascular coupling (NVC), remain debated and are likely to differ depending on the physiological context. Recent evidence points to astrocytes, a cell type possessing specialized protrusions called “endfeet”, that envelop the entire brain vascular tree. Contacts between synapses and endfeet have recently been reported, positioning the latter as ideal mediators of NVC. Here, we developed a computational model that simulates the signaling between neurons, astrocytes, and blood vessels. Our

model successfully reproduces experimental recordings of blood vessels dilation in the brains of awake mice. Our simulations suggest that a specific signaling pathway in astrocytes, involving a molecule called prostaglandin E2, is a key driver of the late phase of NVC, occurring a few seconds after neuronal activity. Furthermore, our model indicates that the location of the stimulated synapses matters: signals sent to the astrocyte endfeet are particularly effective at controlling blood flow. This work helps clarify the active role of astrocytes in brain blood flow regulation, a process critical for healthy brain function.

Introduction

Neurovascular coupling (NVC), the local dilation of blood vessels (also called hyperemia) in response to neuronal activity, is essential for brain function. It sustains neuronal activity by meeting the metabolic needs of neurons, and may have broader roles [1]. This coupling underlies the blood-oxygen-level-dependent (BOLD) signal, measured in functional magnetic resonance imaging (fMRI) [2]. Importantly, vascular dysfunctions or neurovascular uncoupling are observed in a wide range of neurological disorders such as Alzheimer's disease, traumatic brain injury, and multiple sclerosis [3–5]. The mechanisms responsible for these NVC deficiencies are not well understood but could pave the way for novel therapeutic strategies. Glutamate release by active glutamatergic neurons is commonly accepted as the trigger of NVC. Numerous vasodilators downstream glutamate have been suggested to contribute to NVC, such as nitric oxide (NO), prostaglandin E2 (PGE2), or potassium ions, to name a few [4]. A meta-analysis on the various signaling pathways mediating NVC suggested that NO is essential to trigger NVC but identified numerous additional contributors to hyperemia, highlighting the complexity of NVC [6]. NVC dynamics may also vary depending on the type of dilated vessels (arterioles vs capillaries) [7]. Moreover, *in vivo* recordings suggest that NVC dynamics are more complex than simple rise and fall kinetics, and may feature two successive phases, referred to as an "early-phase" and a "late-phase" [8, 9].

Recent studies suggest that neurons are not the only cell types involved in NVC [10]. In particular, astrocytes, glial cells known to interact with neurons and blood vessels, are perfectly positioned to mediate NVC. They possess specialized subcellular compartments, referred to as endfeet, that wrap and cover almost the entire brain vasculature [11]. The involvement of astrocytes in NVC is usually evaluated using their intracellular Ca^{2+} signals as a proxy but remains controversial [12]. Some studies suggest that astrocytes Ca^{2+} elevations are not mandatory to dilate blood vessels [13–15], while others have detected systematic astrocyte Ca^{2+} signals preceding hyperemia, notably in endfeet [16–18]. This apparent discrepancy might result from differences in temporal resolution or from local variability of the neuro-gliovascular unit [19, 20].

Computational models are especially useful in this type of situation, thanks to their ability to disentangle the contributions of the various actors of the system. While most computational models of NVC do not take astrocytes into account [21], several proposals have incorporated them via their Ca^{2+} dynamics [22–27]. However, to the best of our knowledge, the existence of two temporal phases of NVC, early and late, is often ignored in these models or remains phenomenologically described [28], which limits mechanistic interpretability of the underlying biological processes. Moreover, the PGE2 pathway is rarely described in details and is often modeled as being entirely driven by Ca^{2+} signals, without explicit intermediate reactions. Lastly, the astrocyte is most often represented as a single compartment, which fails to account for the extreme

subcellular organization of these cells (endfeet, branchlets, leaflets), thereby neglecting their spatial and functional heterogeneity.

To deepen our understanding of the role of astrocytes in NVC, we developed a mean-field computational model of astrocyte-dependent NVC, implemented using Ordinary Differential Equations (ODEs). The model includes an astrocyte and a blood vessel compartment, as well as a phenomenological neuronal nitric oxide (NO) pathway, that accounts for the early phase observed in *in vivo* arteriole diameter recordings [8]. To model the astrocyte compartment, we first analyzed recent translatome and proteomics datasets [29–32], which revealed that all of the enzymes and receptors of the PGE2 pathway are expressed by astrocytes, in particular in endfeet. Our model successfully reproduces the early and late phases of NVC reported *in vivo* [8]. Using extensive simulation campaigns, we show that the model predicts that the astrocyte PGE2 pathway is sufficient to sustain the late phase of NVC but cannot trigger the early phase. Moreover, our results suggest that PGE2-induced arteriole dilation can occur in the absence of astrocyte Ca^{2+} signals, although the latter amplify NVC. Finally, a spatial implementation of the model in a simplified multi-compartmental astrocyte geometry reveals that the influence of the astrocyte PGE2 pathway on NVC strongly depends on the location of the neuronal input relative to the astrocyte tree. In particular, arteriole dilation is predicted to be strongly reduced when neuronal stimulation occurs elsewhere than at the endfoot.

Materials and Methods

Neurovascular coupling is modeled using ordinary differential equations that couple neuronal activity, astrocyte PGE2 signaling, and vascular diameter dynamics. The complete kinetics scheme of the model is shown in Figure 1. The simulated fluxes are illustrated in supplementary figure S3.

Neuronal activity model

Neuronal NO release is modeled as a phenomenological component capturing the early and rapid vasodilatory contribution observed experimentally [8] without additional mechanistic complexity. More specifically, it corresponds to a rectangular function, active for the first four seconds of stimulation (see figure 2B).

In line with experimental measurements of glutamate concentration dynamics in the synaptic cleft [36], neuronal glutamate release is modeled as an exponential decay with a decay constant $\tau_{\mathrm{G}} = 0.003\ \mathrm{s}^{-1}$, combined with discrete presynaptic releases occurring at regularly-spaced spike times t_{spike}:

$$\frac{d[G]}{dt} = -\frac{[G]}{\tau_G} + \nu_G \delta(t - t_{spike}) \tag{1}$$

where G is the extracellular glutamate concentration, ν_G the glutamate concentration increase occurring at each t_{spike} and $\delta(t)$ is the Dirac delta.

Spike frequency is set at 0.1 Hz and 10 Hz for rest and during neuronal stimulation, respectively [37]. Figure 2A displays representative temporal traces of [G] when the neurons are at rest or during stimulation.

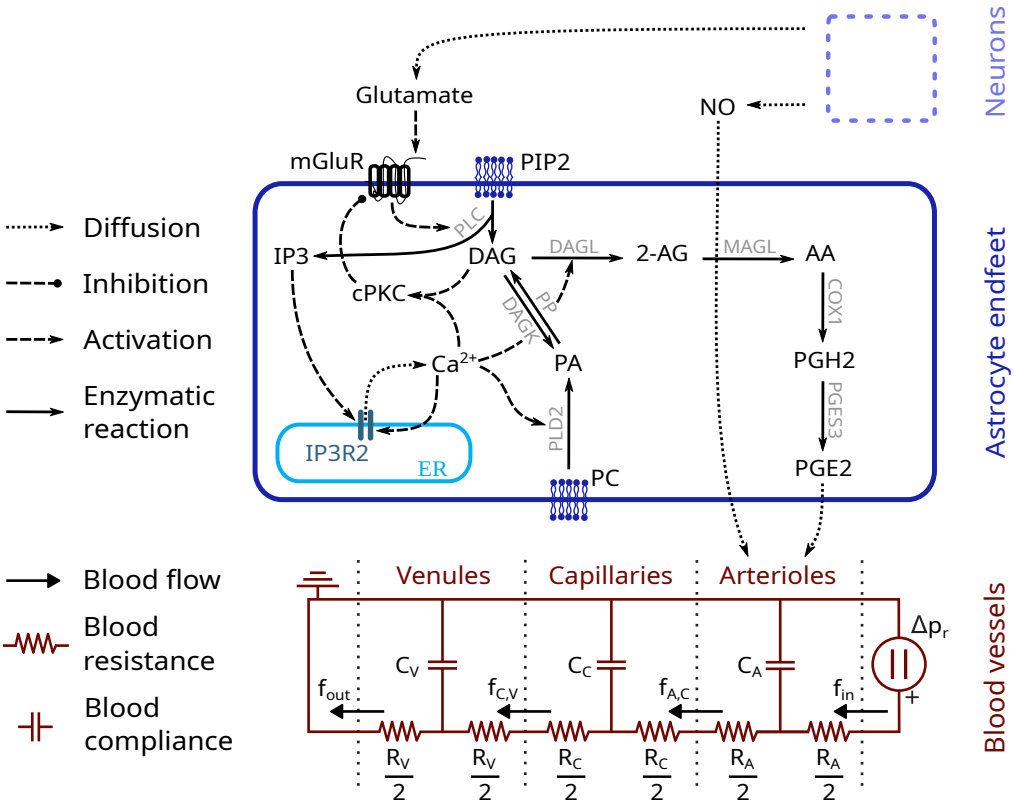

Fig 1. Reaction scheme of the neurovascular coupling model. Neurons release NO and glutamate in the extracellular space. The latter binds to astrocyte mGluRs, triggering calcium-induced calcium release (extended from [33]) and PGE2 production. PGE2, in addition to NO, diffuses to the arterioles, resulting in their dilation. Blood vessels are modeled using an extended 3-compartments Windkessel model [28, 34, 35].

Astrocyte endfoot model

Identification of the astrocyte reaction scheme

Analysis of recent translatome [29] and proteomics data [30–32] revealed that astrocytes and in particular endfeet are enriched in all proteins of the prostaglandin E_2 (PGE2) pathway except Cyclooxygenase 2 (COX2) (Table 1). IP_3R2, mGluR5, PLCβ, DAGLα, PLD2, and COX1 were found enriched in endfeet in at least one database while PP, MAGL, and PGES3 were expressed in the entire astrocyte with not overexpression in endfeet, and PLCδ was statistically more expressed in other compartments than in endfeet.

To facilitate the exploration of these datasets, we provide a script that queries and aggregates the data from these four studies. The code is available here.

From these expression data, we identify two main sources of PGE2 synthesis in astrocytes: phosphatidylcholine (PC) and phosphatidylinositol 4,5-bisphosphate (PIP2) [7, 38–45]. PC is hydrolyzed by phospholipase D2 (PLD2) into phosphatidic acid (PA) [38]. Both PA [39] and PIP2 [40] are substrates for diacylglycerol (DAG) production, which leads to PGE2 production by successive enzymatic reactions, which we will refer to as the PGE2 cascade. PA and PIP2 degradation into DAG are respectively catalyzed by phosphatidate phosphatase (PP) and phospholipase C β (PLCβ) or δ (PLCδ). PLCβ is activated by glutamate binding to mGluR while PLD2 is activated by Ca^{2+} [46]. PGE2 cascade then occurs according to the following steps:

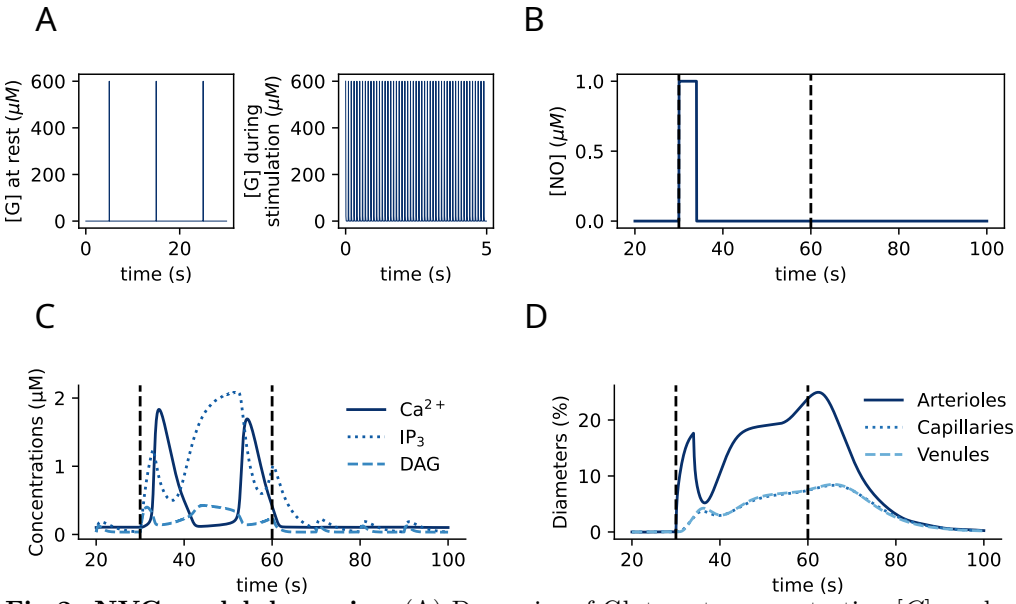

Fig 2. NVC model dynamics. (A) Dynamics of Glutamate concentration $[G]$, under resting (left) and stimulation (right) conditions. (B) Dynamics of NO concentration $[NO]$, modeled as a rectangular function of time. (C) Representative temporal traces of astrocyte calcium-induced calcium release-related variables : Ca^{2+} , IP_3, and DAG concentrations. (D) Representative temporal traces of diameter changes of arterioles, capillaries, and venules, expressed as a percentage of the steady state diameter. In all panels, black vertical dashed lines delineate the stimulation period.

DAG is converted into 2-Arachidonoylglycerol (2-AG) by diacylglycerol lipase (DAGL) [44], followed by arachidonic acid (AA) production by monoacylglycerol lipase (MAGL) [45], prostaglandin H_2 (PGH2) synthesis by COX1 or COX2 [41], and PGE2 production by prostaglandin E synthase 3 (PGES3) [42]. The reaction scheme is depicted in Fig 1. We model it here using the set of differential equations described in the next subsections.

Astrocyte Ca^{2+} and PGE2 signaling model

Calcium-induced calcium release model

Since PGE2 production is partly Ca^{2+} -dependent via PLD2 activation and because mGluR activation triggers calcium-induced calcium release (CICR), we included CICR in the model, using the G-ChI model proposed in refs [33, 47]. The G-ChI model is an extension of the Li-Rinzel model [48] that takes into account the dynamics of $[IP3]$, and its Ca^{2+} -dependence. It describes the dynamics of the following variables: astrocyte cytosolic calcium concentration ($[Ca^{2+}]$), IP_3 concentration ($[IP3]$), IP_3R2 opening probability (h), DAG concentration ($[DAG]$), classical protein kinase C concentration ($[cPKC]$), fraction of activated mGluRs (Γ), and extracellular glutamate concentration ($[G]$). The equations and parameter values of this model can be found in supplementary materials S1 and table S1, respectively. Representative temporal traces of $[Ca^{2+}]$, h, and $[IP_3]$ are shown in figure 2C.

We introduce here an extension of the model, called "PG-ChI", which additionally

Table 1. Summary of the expression of genes or proteins of the PGE2-pathway in four astrocyte omics datasets: Boulay et al. [29] (ribosome-bound mRNAs), Soto et al. [32] (proteomics), Stokum et al. [31] (proteomics), and Hill et al. [30] (proteomics). - : not found, e : found and statistically more expressed in endfeet, a : found and statistically more expressed in non-endfoot compartments, p : found, with no preferential location.

Molecule	gene	Boulay	Soto	Stokum	Hill
mGluR5	grm5	p	p	-	e
IP3R2	IP3R2	-	-	p	e
$PLC\delta$	plcd1	a	a	a	-
	plcd3	p	-	-	-
	plcd4	a	-	-	-
$PLC\beta$	plcb1	a	e	p	-
	plcb2	-	-	-	-
	plcb3	p	-	p	-
	plcb4	e	-	-	-
PLD2	pld2	p	a	-	e
Phosphacidate phosphatase	Lpin1	p	-	a	-
	Lpin2	p	-	-	-
DAGL	dagla	p	-	-	e
	daglb	-	-	-	e
MAGL	mgll	a	p	p	-
COX1	COX1	-	-	e	-
COX2	COX2	-	-	-	-
Prostaglandin E synthase 3	ptges3	a	a	p	-
	ptges2	p	-	p	-
NOS	NOS1	-	p	-	-
	NOS2	-	-	-	-
	NOS3	-	-	e	e

takes into account the contribution of PA to DAG production:

$$J_{PA} = \nu_{PP} \frac{[PA]}{[PA] + K_{PP}} \tag{2}$$

PLD2 activity, catalyzing PA synthesis from PC, is Ca^{2+} -dependent [46, 49]. To account for this regulation, we assume that Ca^{2+} modulates PLD2 activity in a saturable manner, consistent with enzyme activation kinetics. We therefore describe PA production by PLD2 using the Hill equation:

$$J_{Ca} = \nu_{PLD} \frac{[Ca^{2+}]^{n_{PLD}}}{[Ca^{2+}]^{n_{PLD}} + K_{PLD}^{n_{PLD}}} \tag{3}$$

The mean field dynamics of PA concentration is thus given by:

$$\frac{d[PA]}{dt} = J_{Ca} + J_D - J_{PA} - \frac{[PA]}{\tau_{PA}} \tag{4}$$

where J_D is the DAGK-mediated PA production rate taken here from the G-ChI model [33].

In the G-ChI model, DAG degradation is described by the J_A term, that takes into account DAG degradation into 2-AG by DAGL and other unknown DAG degradation mechanisms, the latter being assumed to be linear by the authors [33]. Here, we introduce an explicit J_{2AG} flux, which corresponds to the rate of DAGL-mediated production. Experimental reports indicated that 2-AG production by DAGL has a Ca^{2+} -dependent and a Ca^{2+} -independent component [43, 44, 50]. We thus combine a basal and a Ca^{2+} -dependent term:

$$J_{2AG} = \frac{[DAG]}{[DAG] + K_{DAGL}} \left(\nu_{DAGL} + \nu_{CaDAGL} \frac{[Ca^{2+}]}{[Ca^{2+}] + K_{CaDAGL}} \right) \tag{5}$$

The mean field dynamics of DAG concentration thus becomes:

$$\frac{d[DAG]}{dt} = J_{PLC\beta} + J_{PLC\delta} + J_{PA} - J_{KP} - J_D - J_{2AG} \tag{6}$$

where $J_{PLC\beta}$ and $J_{PLC\delta}$ are the DAG production terms by PLC β and δ, respectively, and J_{KP} is the cPKC production term [33].

PGE2 cascade

The PGE2 cascade is modeled here with the following ODEs:

$$\frac{d[2AG]}{dt} = J_{2AG} - J_{AA} - \frac{[2AG]}{\tau_{2AG}} \tag{7}$$

$$\frac{d[AA]}{dt} = J_{AA} - J_{PGH2} - \frac{[AA]}{\tau_{AA}} \tag{8}$$

$$\frac{d[PGH2]}{dt} = J_{PGH2} - J_{PGE2} - \frac{[PGH2]}{\tau_{PGH}} \tag{9}$$

$$\frac{d[PGE2]}{dt} = J_{PGE2} - \frac{[PGE2]}{\tau_{PGE}} \tag{10}$$

where:

$$J_{AA} = \nu_{MAGL} \frac{[2AG]}{[2AG] + K_{MAGL}} \tag{11}$$

$$J_{PGH2} = \nu_{COX} \frac{[AA]}{[AA] + K_{COX}} \tag{12}$$

$$J_{PGE2} = \nu_{PGE} \frac{[PGH2]}{[PGH2] + K_{PGE}} \tag{13}$$

We could not find quantitative experimental data for MAGL kinetics. We therefore assume that MAGL-mediated 2-AG hydrolysis operates much faster than DAGL-mediated production. Thus, 2-AG dynamics is considered at quasi-steady state and $\frac{d[2AG]}{dt} \simeq 0$. Neglecting 2AG degradation, i.e. $\frac{[2AG]}{\tau_{2AG}} = 0$, we obtain $J_{2AG} \simeq J_{AA}$. Thus, the mean field dynamics of AA concentration, eq.(8) above, becomes:

$$\frac{d[AA]}{dt} = J_{2AG} - J_{PGH2} - \frac{[AA]}{\tau_{AA}} \tag{14}$$

The combined PG-ChI and PGE2 cascade equations, eqs. (2)-(7) and (9)-(14), are referred to as the PG-ChI–PGE2 model. Parameter values of the PGE2 cascade model are listed in table 2 and parameter values of the G-ChI model in Supplementary table S1. The fluxes of the astrocyte Ca^{2+} and PGE2 signaling model are depicted in supplementary figure S3.

Table 2. Parameter values of the PGE2 cascade model.

Parameter	Description	Value	Unit	Reference
PLD2 activity				
ν_{PLD}	Maximal rate of PA production	1.2	μM.s^{-1}	-
$\mathrm{K_{PLD}}$	Ca^{2+} affinity to PLD2	0.2	μM	-
$\mathrm{n_{PLD}}$	Hill coefficient of PA production	2	-	-
PP activity				
ν_{PP}	Maximal rate of DAG production from PA	5	μM.s^{-1}	-
$\mathrm{K_{PP}}$	PA affinity to PP	12	μM	[39]
DAGL activity				
ν_{DAGL}	Maximal rate of Ca^{2+} -independent AA production	0.055	μM.s^{-1}	-
$\mathrm{K_{DAGL}}$	DAG affinity to DAGL	75	μM	[44]
ν_{CaDAGL}	Maximal rate of Ca^{2+} -dependent AA production	1	μM.s^{-1}	-
$\mathrm{K_{CaDAGL}}$	Ca^{2+} affinity to DAGL	2.4	μM	-
COX1 activity				
ν_{COX}	Maximal rate of PGH2 production	1	μM.s^{-1}	-
$\mathrm{K_{COX}}$	AA affinity to COX1	10	μM	[41]
PGES activity				
ν_{PGE}	Maximal rate of PGE2 production	1.5	μM.s^{-1}	-
$\mathrm{K_{PGE}}$	PGH2 affinity to PGES3	14	μM	[42]
cAMP production				
ν_{cAMP}	Maximal rate of cAMP production	2	μM.s^{-1}	-
$\mathrm{EC_{50}}$	PGE2 affinity to EP_4 receptors	0.0003	μM	[51]
Decay times				
τ_{PA}	PA decay time	0.5	s	-
τ_{AA}	AA decay time	2	s	-
τ_{PGH}	PGH2 decay time	disregarded	s	-
τ_{PGE}	PGE2 decay time	1	s	-
τ_{cAMP}	cAMP decay time	1	s	-

Vasculature model

To model the impact of PGE2 release on blood vessel diameter, a vasculature compartment was added to the endfeet compartment described above. The model is an extension of the three-compartment Windkessel model, developed by previous computational studies [28, 34, 35, 52]. It consists of an electrical circuit analogy that describes the mean field dynamics of the relative volumes of arterioles (V_a), capillaries (V_c), and venules (V_v):

$$\frac{dV_a}{dt} = \frac{1}{k_{vis,a}}\Big(\frac{K_a - \frac{V_a}{V_{a,0}}}{K_a - 1} + E - \frac{2}{C_{a,0}}\frac{V_a}{(r_1 + r_2)\cdot f_1 + (r_2 + r_3)\cdot f_2 + r_3 f_3}\Big) \tag{15}$$

$$\frac{dV_c}{dt} = \frac{1}{k_{vis,c}}\Big(\frac{K_c - \frac{V_c}{V_{c,0}}}{K_c - 1} - \frac{2}{C_{c,0}}\frac{V_c}{(r_2 + r_3)\cdot f_2 + r_3 f_3}\Big) \tag{16}$$

$$\frac{dV_v}{dt} = \frac{1}{k_{vis,v}}\Big(\frac{K_v - \frac{V_v}{V_{v,0}}}{K_v - 1} - \frac{2}{C_{v,0}}\frac{V_v}{r_3 f_3}\Big) \tag{17}$$

Assuming all blood vessels are cylinders of constant height, their relative diameter dynamics is given by:

$$\Delta D = \frac{dD}{dt} = \sqrt{\frac{V}{V_0}} - 1 \tag{18}$$

where V is the relative vessel volume and V_0 the basal value of the relative vessel volume. Representative temporal traces of arterioles, capillaries, and venules relative diameters are shown in figure 2D.

The influence of external factors on blood vessel radius is described by E, which is defined in the next subsection. Parameter values of the vasculature model were taken from [28] and are displayed in supplementary table S2.

Coupling of neuron, astrocyte, and vascular dynamics

Arteriole smooth muscle cells express four G protein-coupled receptor subtypes that are activated by PGE2: EP_{1-4}. EP_2 and EP_4 activation triggers vasodilation [53, 54]. EP_4 is weakly expressed in cerebral arteriolar smooth muscle cells (SMCs) [55, 56], whereas EP_2 does not seem to be expressed. Similar observations were made in human middle cerebral arteries [54]. We therefore restrict the focus of our model to EP_4.

EP_4 activation by PGE2 results in an increase of $cAMP$ concentration in the SMC [51, 57], so that the mean field dynamics of cAMP concentration can be described as:

$$\frac{d[cAMP]}{dt} = \nu_{cAMP}\frac{[PGE2]}{[PGE2] + EC_{50}} - \frac{[cAMP]}{\tau_{cAMP}} \tag{19}$$

cAMP then inhibits Myosin-Light-Chain phosphatase (MLCP) via PKA stimulation, which in turn phosphorylates MLCP, resulting in cytosolic Ca^{2+} decrease and subsequent vessel dilation [58–60]. Since this mechanism is not fully understood we model the influence of cAMP concentration in vascular SMC $[cAMP]$ on arteriole diameter as a Hill function with exponent n_c. In addition to cAMP, the arteriole diameter is also directly impacted by neuronal NO production. The influence of neuronal and astrocyte activity on arteriole diameter (term E in eq.(15) above) is therefore modeled as:

$$E = O_c\frac{[cAMP]^{n_c}}{K_{cAMP}^{n_c} + [cAMP]^{n_c}} + O_n[NO] \tag{20}$$

where O_c is the maximal cAMP effect on arteriole dilation, K_{cAMP} is the half cAMP activation concentration, and O_n is the maximal NO effect on arteriole dilation.

Spatial model

To assess the impact of the location of neuronal stimulation on astrocyte-mediated NVC, we spatialized the astrocyte compartment using the finite volumes method [61]. Astrocyte geometry was simplified into three compartments: a soma, an endfoot, and two leaflets connected by branches (Figure 6A). Branches are themselves made of cylinders sharing the same diameter d. Each portion of a branch connecting two compartments (endfoot, soma, leaflets), or a compartment and an intersection between two branches, is divided into ten cylindrical subcompartments.

The endfoot volume was set to 2.0 μm^3 based on unpublished 3D endfoot reconstructions from Focused Ion Beam-Scanning Electron Microscopy (FIB-SEM) data (courtesy from Prof. K. Murai, McGill University, Montreal, Canada). The diameter of the astrocytic soma was estimated based on a confocal image of an astrocyte expressing GCaMP6f from Covelo et al. (ref [62], Fig.1). Since the soma was modeled as a sphere, its volume was set to 4200 μm^3. Lastly, the volume of the leaflets was set to 0.4 μm^3, based on FIB-SEM data of leaflet perisynaptic astrocytic processes [63, 64]. These parameter values are listed in table 3. The values of branches diameter d and lengths L_1 and L_2 varied in our simulations to reflect their experimentally reported variability: from 10-200 nm (branchlets) to 1-2 μm (branches) in diameter and up to 20 μm in length [62, 65] (table 4).

All subcompartments (endfoot, soma, leaflets, and cylinders) are coupled via one-dimensional Ca^{2+} and IP_3 diffusion. According to Fick's first law, the molar flux density j is proportional to the concentration gradient ∇C:

$$j = -D_C \nabla C \tag{21}$$

where D_C is the diffusion coefficient.

Assuming one-dimensional diffusion along the x-axis, the equation becomes:

$$j = -D_C \frac{\partial C}{\partial x}$$

Let S denote the exchange surface between two neighboring compartments. The total molar flux across this surface is then given by:

$$\Phi = \iint_S j dS$$

Considering a uniform flux density over the surface, this expression simplifies to:

$$\Phi = j * S = -D_C S \frac{\partial C}{\partial x}$$

The mean-field dynamics of the molecule concentration in compartment i C_i, which is coupled by diffusion to compartments $i+1$ and $i-1$ is thus given by:

$$\frac{dC_i}{dt} = D_C \frac{C_{i-1} + C_{i+1} - 2C_i}{(\Delta x)^2} \tag{22}$$

where Δx is the distance between neighboring compartments. See supplementary materials S2 for further details.

Table 3. Constant geometrical parameter values of the spatial model. Length is the compartment size along the diffusion axis. The whole astrocyte geometry is displayed in Fig 6.

Compartment	Volume (μm^3)	Length (μm)
Soma	4200	20
Endfoot	2	1
Leaflets	0.4	0.1

Table 4. Varying geometrical parameter values of the spatial model. These parameters describe the sizes of branches connecting the somatic, endfoot, and leaflet compartments. Branches are modeled as cylinders. The whole astrocyte geometry is displayed in Fig 6.

Parameters	L_1	L_2	d
Variation interval (μm)	1-20	1-15	0.02-2

Assuming that DAGL is only expressed in endfeet (see table 1), the set of reactions occurring in the endfoot compartment was described by the PG-ChI–PGE2 model, whereas the PG-ChI model was implemented in the other compartments, including branches.

Simulations

We used the solve_ivp function from the scipy.integrate library, with the Radau algorithm, to simulate the dynamics of the well-mixed system (18 ODEs) and the spatialized model (282 ODEs). The code, implemented in Python, is available here. Parameter values were taken, whenever possible, from the literature. The remaining parameters were calibrated to fit experimental arteriole ΔD traces, within biologically plausible ranges: maximal rate of molecules production were chosen between 0.01 and 10 $\mu M.s^{-1}$; decay times were taken between 0.1 and 5 s, or disregarded, whenever possible, for model simplicity. Model dynamics was computed at rest conditions (no neuronal stimulation), until the equilibrium was reached ($\approx$ 50 s simulation time). The steady state values were used as the initial conditions of all the simulations presented in this study.

Data analysis

The Root Mean Squared Error (RMSE) was computed using numpy to quantify the distance between virtual and experimental ΔD. The bifurcation analysis was computed with the XPPAUT software. For computational simplicity, $[G]$ was treated as a constant parameter for the bifurcation analysis (bifurcation parameter), instead of the pulsatile input of the full model.

Results

The model successfully reproduces *in vivo* arteriole dilation dynamics

To study the role of astrocytes in NVC, we have developed an ODE model that couples glutamatergic neuronal activity, astrocyte activity, and blood vessel diameter variations. The reaction scheme of this model is presented in Figure 1. The model of astrocyte activity was chosen based on astrocyte translatome (ribosome-bound mRNAs, [29]) and

proteomics datasets [30–32] and couples the Ca^{2+} and PGE2 signaling pathways. Astrocyte Ca^{2+} activity was implemented based on the G-ChI model [33, 47], which simulates Ca^{2+} -induced Ca^{2+} release. The extension proposed here, referred to as the PG-ChI-PGE2 model, additionally accounts for the PGE2 signaling pathway as well as PA-mediated DAG production. Neuronal activity is modeled as a release of glutamate and NO, as the latter has been reported to partly mediate NVC [66, 67]. An extended three-compartments Windkessel model was implemented to simulate the dynamics of blood vessel diameter change, as done in previous computational studies [28, 34, 35, 52]. The model is implemented as a set of eighteen ordinary differential equations (see Methods section). Parameter values were taken from the literature when available and manually set otherwise (see table 2, and supplementary materials S1 and S2).

To validate the model, we first compared its dynamics with *in vivo* mice arteriole diameter recordings from Institoris et al. [8] (Figure 3). To investigate the role of astrocytes in NVC, Institoris et al. [8] used Adeno-Associated Viruses expressing a plasma membrane Ca^{2+} ATPase targeting astrocytes (CalEx), which reduces evoked and spontaneous elevations of free Ca^{2+} in astrocytes [68]. In the model, CalEx conditions were simulated by setting $d[Ca^{2+}]/dt = 0$. The simulated relative arteriole radius variations, ΔD closely matched the experimental traces in control conditions under sustained neuronal stimulation (30 s), with a root mean squared error (RMSE) of 2.5 (Figure 3B). For short neuronal stimulations (5 s), the simulated traces qualitatively reproduced the experimental data, but the fit displayed a larger RMSE of 5.4 (Figure 3 A). The model was able to capture both the "early-phase" (from stimulation onset to $\approx$ 2-4 s post-stimulation) and the "late-phase" of NVC (from 5-7 s post-stimulation onset to stimulation termination). Interestingly, the model was also able to reproduce ΔD dynamics with reduced astrocyte Ca^{2+} activity (CalEx) under either short (Figure 3C, RMSE=4.0) or long (Figure 3D, RMSE=3.38) neuronal stimulation. Both simulation and experimental CalEx traces were characterized by a decreased blood vessel radius dilation compared to control conditions during the late-phase of NVC. Note that vessel dilation was delayed by a few seconds in the CalEx simulations under short stimulation duration, which explains the increased RMSE between simulated and experimental data in these conditions. Importantly, the simulated radius dynamics following short neuronal stimulation displays a secondary radius dilation peak that is delayed compared to experimental traces (Figure 3A). As it is virtually absent from the simulated CalEx trace (Figure 3C), the second peak is likely mediated by astrocyte Ca^{2+} signaling.

The PGE2 pathway triggers the late phase of NVC

In order to investigate the contribution of the astrocyte PGE2 and neuronal NO pathways to NVC, we ablated each pathway from the model independently, yielding the "PGE2-KO" and "NO-KO" models, respectively. While the NO pathway allowed for rapid diameter dilation displaying similar characteristics to the "early-phase" of NVC, the PGE2 pathway triggered a slower and delayed dilation reminiscent of the "late-phase" of NVC, both in control and CalEx conditions (Figure 4A). To gain a better understanding of the contribution of each element of the PGE2 pathway to NVC, we knocked out specific enzymes of the signaling cascade by setting their maximum production rate value to 0 (Figure 4B). Notably, inhibiting PLD2 activity (ν_{PLD}=0 in equation 3) resulted in a decrease of the maximum value of ΔD. Note that knocking down PP ($\nu_{PP} = 0$ in equation 2) had similar effects (fused curves; not shown).

Then, we studied the influence of $PLC\beta$- and $PLC\delta$-mediated DAG production on NVC. First, we knocked out both PLC isoforms, ($\nu_\delta = 0$ and $\nu_\beta = 0$). To specifically evaluate the role of DAG on NVC, parameter values were only modified for DAG

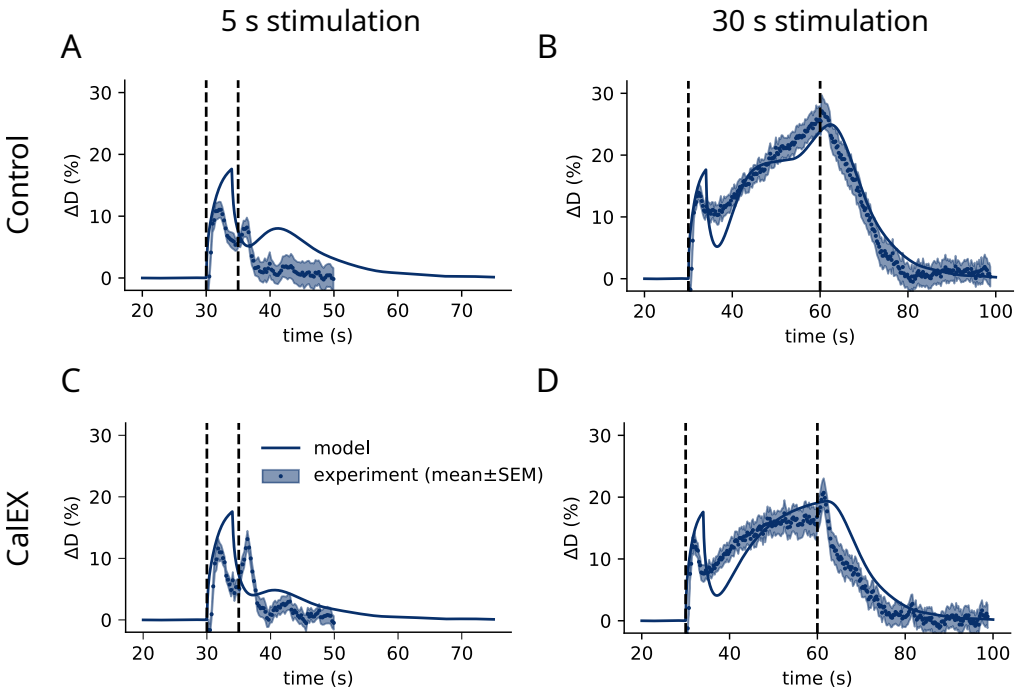

Fig 3. The model successfully reproduces *in vivo* experimental arteriole diameter dynamics. Temporal variations of the simulated relative arteriole radius (dark blue line), ΔD, in control (top, A-B) and CalEX (bottom, C-D) conditions, under 5 s (left, A,C) and 30 s (right, B,D) neuronal stimulation. Experimental traces from Institoris et al. [8] are displayed as mean values (blue dots) ± SEM. Black vertical dashed lines delimit the neuronal stimulation period.

production, whereas those for IP_3 production were kept unchanged. Surprisingly, most of the diameter dilation was abolished in the "late-phase", with ΔD reaching lower values than when knocking down PLD2. In this model, $PLC\beta$ strongly influences NVC while $PLC\delta$ has minimal effects, as shown by the specific effect of $PLC\beta$ and $PLC\delta$ KO (Figure 4B). This is not surprising as ν_β is about ten times larger than ν_δ [33], which is consistent with the low expression of $PLC\delta$ in endfeet compared to the rest of the astrocyte (table 1). Note that suppressing $PLC\delta$-mediated production of both DAG and IP_3 was not significantly different from suppressing $PLC\delta$-mediated DAG production alone (fused curves; not shown). In contrast, inhibiting both $PLC\beta$-mediated IP_3 and DAG production completely abolished the "late-phase" of NVC (not shown).

To evaluate the respective roles of the Ca^{2+} -dependent and Ca^{2+} -independent DAGL activity in NVC, we respectively set ν_{CaDAGL} and ν_{DAGL} to 0. Knocking down ν_{DAGL} resulted in a decreased maximum ΔD by roughly 30 %. The amplitude of vessel diameter oscillations was about 75 % higher than in control conditions, as in the latter ΔD oscillations are smoothed by the Ca^{2+} -independent DAGL effect. In contrast, suppressing the Ca^{2+} -dependent DAGL effect ν_{CaDAGL} altered ΔD oscillations by reducing the maximal amplitude of ΔD by 80 %.

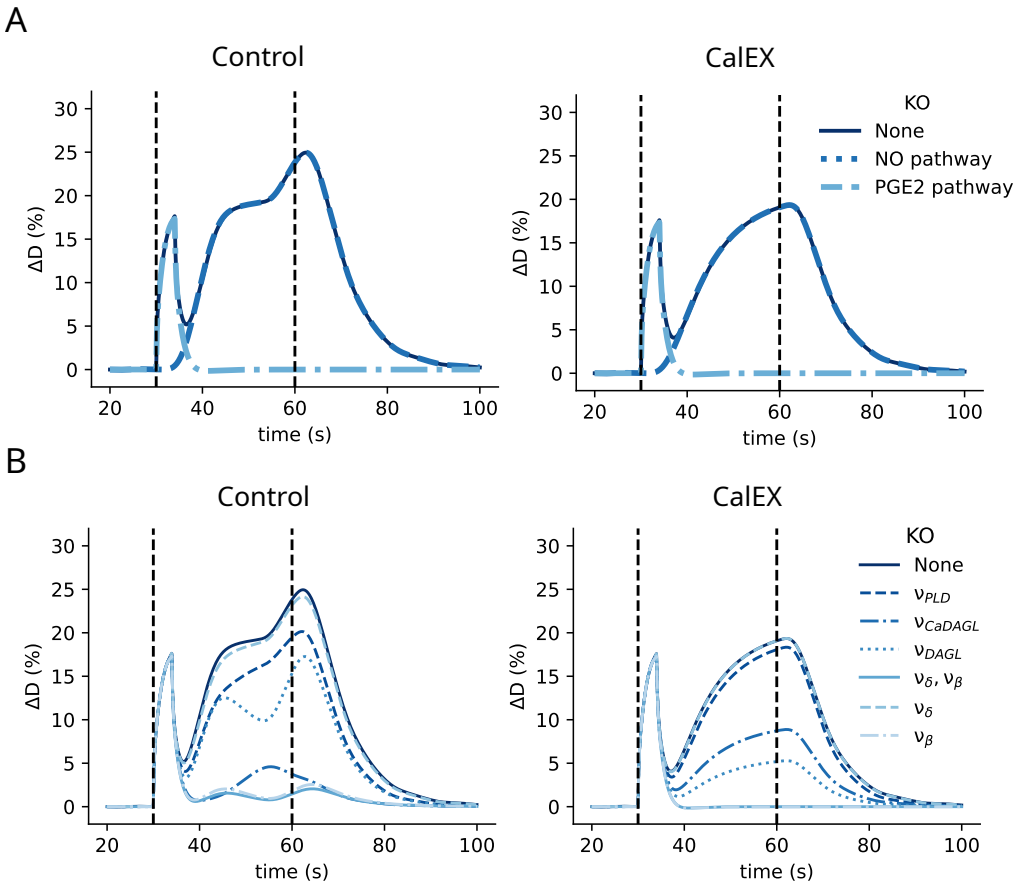

Fig 4. Study of the contribution of modeled reactions to the different phases of NVC. (A) Comparison of the temporal variations of the relative arteriole radius, ΔD, in the control (dark blue line), NO-KO (blue dotted line) and PGE2-KO (light blue dash-dotted line) models in control (left) and CalEX (right) conditions. (B) Temporal variations of ΔD for another set of virtual KOs: ν_{PLD}-KO, ν_{DAGL}-KO, ν_{CaDAGL}-KO, ν_{δ}-KO, and ν_{β}-KO models in control (left) and CalEX (right) conditions. Black vertical dashed lines delimit the neuronal stimulation period.

Increased extracellular neuronal glutamate release results in larger arteriole dilation and astrocyte Ca^{2+} oscillations

As our results suggest that glutamate is causal to the "late-phase" of NVC (Figure 4, we hypothesized that the amount of neuronal glutamate released at the vicinity of the astrocyte should strongly impact astrocyte activity and blood vessel dilation. To test this hypothesis, we ran simulations with varying values of ν_G, the peak glutamate concentration occurring at each stimulation time t_{spike} (equation 1). As expected, decreasing ν_G did not affect the early-phase of NVC but resulted in a reduced "late-phase" maximum relative arteriole diameter. For example, a 80 % decrease in ν_G resulted in a 60 % decrease in the maximum "late-phase" ΔD (Figure 5A). Moreover, a tenfold decrease in glutamate amplitude completely supressed the second peak of ΔD. A bifurcation analysis of the system reveals that a subcritical Hopf bifurcation occurs when the extracellular glutamate concentration $[G]$ reaches about 2.4 μM (Figure 5B). Above this value, $[Ca^{2+}]$, $[IP_3]$ and $[DAG]$ oscillate, leading to the observed ΔD oscillations.

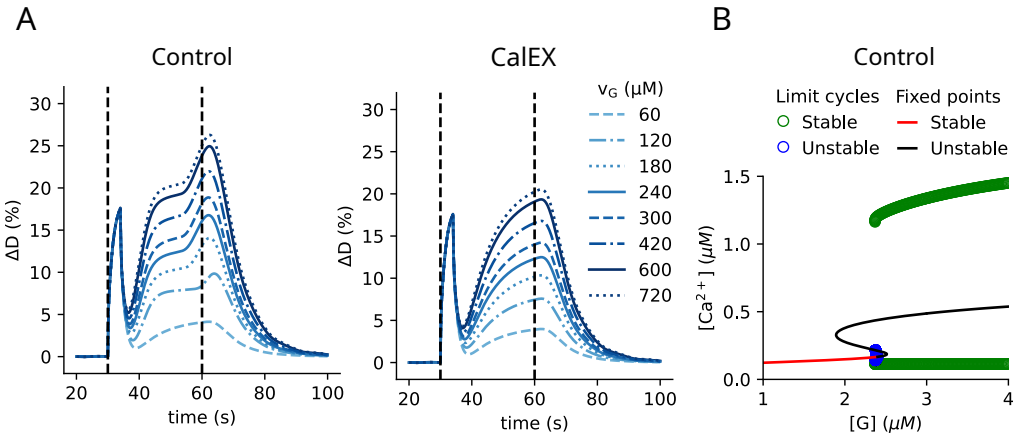

Fig 5. Extracellular glutamate concentration governs arteriole dilation and astrocyte Ca^{2+} oscillations. (A) The peak extracellular glutamate concentration, ν_G, strongly impacts the relative blood vessel diameter variations, ΔD, following neurostimulation in control (left) and CalEX (right) conditions. ΔD oscillations can be observed from $\nu_G = 120\ \mu M$, in control conditions only. Black vertical dashed lines delimit the stimulation period. (B) Bifurcation diagram of the model with the extracellular glutamate concentration $[G]$ as a bifurcation parameter. A subcritical bifurcation appears for $[G] \approx 2.4\ \mu$M, giving rise to an unstable (blue circles) and a stable limit cycle (green circles). The unstable fixed point (black line) resulting from the Hopf bifurcation however coexists with two other unstable fixed points. The unstable limit circle collides with the intermediate unstable fixed point close to the Hopf bifurcation.

Peri-endfoot glutamatergic release enhances astrocyte PGE2-mediated NVC

Different astrocyte compartments, including endfeet, have recently been reported to contact synapses by Aten et al. (ref. [69] Fig. 6). Therefore, we next investigated the impact of the location of active synapses on astrocyte-mediated NVC. To do so, we implemented a spatial model of astrocyte-dependent NVC. The astrocyte in our spatial model is composed of the following compartments: a soma (S), an endfoot (Ef), leaflets (F_1 and F_2), and branches of diameter d and lengths L_1 and L_2, coupled by Ca^{2+} and IP_3 diffusion (Figure 6A). DAG, a membrane lipid, was not considered a diffusing molecule [70, 71]. In accordance with recent astrocyte omics data suggesting that DAGL and COX1 are only expressed in endfeet (table 1), the PGE2 signaling cascade was only implemented in the endfoot (PG-ChI–PGE2 model, see Methods section for details). To explore the impact of astrocytes on NVC depending on the nature and spatial distribution of the stimulated compartment, simulations were run for different values of d, L_1, and L_2, following either somatic (S), endfoot (Ef), or leaflet (F_1 or F_2) stimulation. Note that since astrocytes only impact the "late-phase" of NVC (Figure 4), only the latter was analyzed in this set of *in silico* experiments.

First, whatever the size of the compartments and parameter values, Ca^{2+} signals were never found to reach the endfoot when neuronal stimulation occurred at leaflets (fig.6D/F_1,F_2). Only soma or endfoot stimulation yielded Ca^{2+} signals that were transmitted to the endfoot (fig.6D/S,Ef). In this case, the influence of branch diameter d on the amplitude of the transmitted Ca^{2+} signal was completely different depending on whether neuronal stimulation occurred at the soma or at the endfoot levels. The amplitude of the endfoot Ca^{2+} signal increased with d for somatic stimulation but

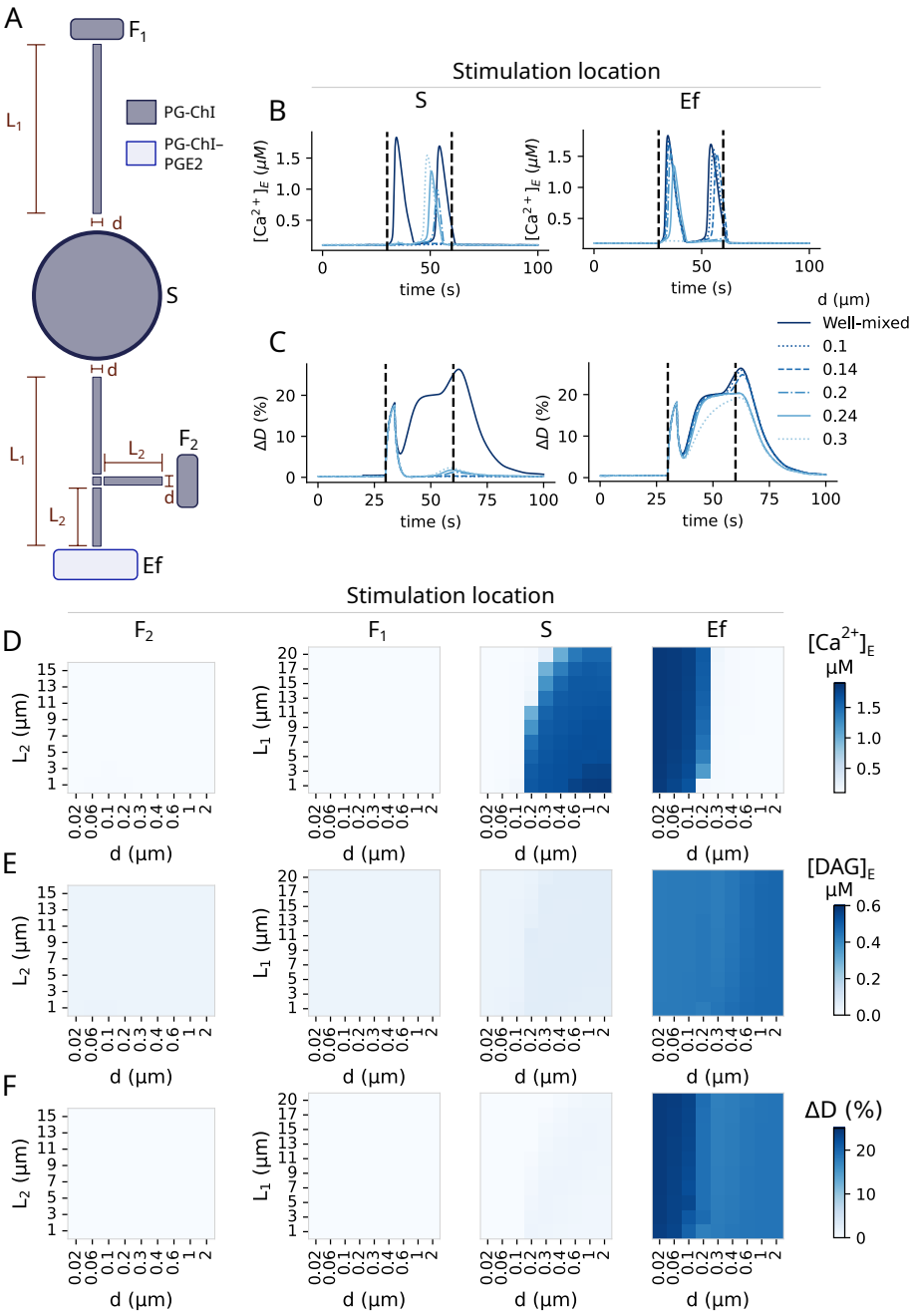

Fig 6. Simulations of the spatial model suggest that astrocyte PGE2-mediated vasodilation only happens when neuronal stimulation occurs at the endfoot level. (A) Schematic representation of the simplified astrocyte geometry in the spatial model. It is composed of a soma (S), an endfoot (Ef), leaflets (F_1 and F_2), and branches of diameter d and lengths L_1 and L_2. Traces of endfoot Ca^{2+} concentration (B) and ΔD (C) for a range of branch diameter d in simulations where either the soma (S, left), or the endfoot (E, right) was stimulated, $L_1 = 11$ μm and $L_2 = L_1/2$. Black vertical dashed lines delimit the neuronal stimulation period. Heatmaps show the peak endfoot concentration of Ca^{2+} ($[Ca^{2+}]_E$, D) and DAG ($[DAG]_E$, E), and the peak relative arteriole dilation (ΔD, F), for different stimulation locations: leaflets (F2 or F1), soma (S), or endfoot (Ef). In *in silico* experiments, L_1 was set to 20 μm when varying L_2. L_2 was set to $L_1/2$ when varying L_1.

decreased with increasing d under endfoot stimulation. Indeed, large values of d facilitate the diffusion of Ca^{2+} from the soma to the endfoot for somatic stimulation, but they facilitate Ca^{2+} diffusion away from the endfoot upon endfoot stimulation. Therefore, our spatial model suggests that endfoot Ca^{2+} signals are favored by large branch diameters if neuronal stimulation happens on the soma whereas they are favored by small branch diameters if neuronal stimulation occurs directly at the endfoot. In contrast, endfoot DAG concentration was barely affected by astrocyte geometry, probably because it does not diffuse.

In strong opposition to Ca^{2+} dynamics, however, endfoot DAG production and blood vessel dilation mainly occurred when the stimulated compartment was the endfoot and not the soma. The smaller the astrocyte branch diameter, the larger the arteriole dilation. More precisely, endfoot stimulation in astrocyte geometries with branch diameter $d < 0.1$ μm displayed relative arteriole diameter increases ΔD similar to the well-mixed model (Figure 6C). Above this value, ΔD decreased to about 15 %. Simulations with values of $d > 0.2$ μm suggest that endfoot DAG concentration increases are sufficient to trigger arteriole dilation even in the absence of Ca^{2+} signals (Figure 6E-F). We also note that somatic stimulation can trigger Ca^{2+} signals in the endfoot that reach levels similar to the well-mixed model, but these somatically-triggered Ca^{2+} signals resulted in minor peaks of endfoot DAG concentration and, consequently, in minor ΔD elevations (under 3 %). Moreover, somatic stimulation failed to trigger the first Ca^{2+} peak compared to the well-mixed implementation, but triggered the second Ca^{2+} peak up to 6 s earlier than the second peak of the well-mixed model (Figure 6B).

Because leaflets have recently been reported to form domains that integrate multiple synapses [72], we next simulated a domain of ten neighboring leaflets at either F_1 or F_2 locations (supplementary figure S1). Only F_2 leaflets activation was able to trigger endfoot [Ca^{2+}] elevations, and only when they were located very close to the endfoot (1 μm). Surprisingly, the influence of branch length on endfoot activity after endfoot or somatic stimulation was larger when multiple leaflets were active (compare supplementary figure S1 with figure 6). This phenomenon is particularly strong for branch diameters ≥ 200 μm. This may result from an increase in the volume of the entire astrocyte with branch length, resulting in an enhanced dilution effect. As in the case of single leaflet activation (figure 6), the arteriole was mainly dilated when stimulation occurred at the endfoot level.

Lastly, we tested scenarios where the PGE2 pathway was expressed in all astrocyte compartments. To this end, we simulated the PG-ChI-PGE2 model in all modeled compartments (supplementary figure S2). As the diffusion coefficients of PA, AA, PGH2, and PGE2 were not available in the literature, they were assumed to equal 300 $\mu m^2.s^{-1}$. This value is an upward estimate, based on the effective Ca^{2+} and IP_3 diffusion coefficients, respectively 13 and 280 $\mu m^2.s^{-1}$ [71]. Under these assumptions, the influence of the soma on NVC was larger than when the PGE2 pathway is restricted to the endfoot, triggering arteriole dilation to levels close to those of the well-mixed model. This effect was however only possible if the soma and the endfoot were connected by large branches (high value of d, figure S2). Conversely, the influence of endfoot activation on arteriolar dilation decreased more rapidly with d than when only endfeet expressed the PGE2 pathway molecules (figure S2 vs. 6). As more molecules are diffusing in this implementation of the model, the dilution effect was amplified.

Taken together, these results suggest that astrocyte geometry plays a significant role

in shaping intracellular diffusion and therefore Ca^{2+} and PGE2 dynamics. Overall, neuronal stimulation at the leaflets level triggered almost no arteriole dilation, regardless of the geometric parameters. Neuronal stimulation at the somatic level could only trigger arteriole dilation if the soma was expressing molecules of the PGE2 pathway; if PA, AA, PGH2, and PGE2 diffused within the astrocyte; and if the diameter of branches connecting the soma to the endfoot was large. Neuronal stimulation at the endfoot level always triggered arteriole dilation, provided that only Ca^{2+} and IP_3 were diffusing, with NVC being optimal when endfeet were connected to thin branches.

Discussion

The roles of astrocytes in NVC remain highly debated. In particular, the involvement of astrocytic Ca^{2+} signals in NVC is controversial. Although Ca^{2+} signals have been observed in endfeet concomitantly with vasodilation [73–75], early studies suggested that these Ca^{2+} transients followed blood vessel dilation temporally, and therefore did not trigger it [14]. More recently, hyperemia has been observed *in vivo* in the absence of IP_3R2-mediated Ca^{2+} signals in astrocytes [13]. In contrast, other *in vivo* experiments in awake mice challenged this view by suggesting that NVC could be partly astrocyte Ca^{2+} -mediated [8, 76]. Here, we have developed a model that accounts for these observations. The model recapitulates the astrocyte-independent early phase and partially astrocyte-dependent late phase of NVC reported by Institoris et al. [8]. The latter is triggered by PLD2 and Ca^{2+} -dependent DAGL activity, as well as Ca^{2+} -independent $PLC\beta$ and DAGL activity. Our model successfully replicates qualitative arteriole diameter variations both in control and CalEx conditions. Whether these two phases of NVC vary depending on blood vessel type, brain region, and other (patho-)physiological sources of variability of the neuro-gliovascular unit remains to be explored.

Neuronal NO is a key player of NVC [6, 67, 77]. It is produced upon N-methyl-D-aspartate (NMDA) receptor activation by the neuronal nitric oxide synthase isoform (nNOS). NO then diffuses and activates soluble guanylate cyclase in neighboring vessel smooth muscle cells, leading to cGMP synthesis, which downstream reactions result in SMC relaxation [5, 77]. Here, as we focus on astrocyte-mediated NVC, NO release is described with a simple phenomenological model. This implementation was enough to obtain good qualitative fitting of the model to *in vivo* experimental traces in awake mice. Interestingly, the relative contribution of NO to NVC varies with local expression levels, which are brain region-dependent [78]. A mechanistic model of neuronal NO signaling and downstream reactions in SMCs could help provide a better quantitative match of the model with experimental traces and take into account this local variability.

Our results suggest that blocking $PLC\beta$ activity should result in a decrease in arteriole dilation during the late-phase of NVC. This is in contrast to experiments on brain slices that reported no reduction in stimulation-evoked capillary dilation following the pharmacological blockage of PLC [7]. This is not entirely surprising as mGluR blockage in this study did not affect endfoot Ca^{2+} activity either. The use of brain slices may have influenced this result since other studies on *in vivo* adult mice [79] or adult rats [74] have shown that astrocyte mGluR5 were partly mediating NVC. As the gliovascular unit varies depending on the developmental stage, brain region, and in disease, together with variations in cell and blood vessel composition, the signaling pathways involved are likely to vary too. For example, glutamatergic axons in the mouse cerebral cortex have been reported to dilate neighboring arterioles via direct

synaptic-like neuron–arteriolar smooth muscle cell communication [80], and astrocytes have been suggested to contribute to NVC at the capillary but not at the arteriolar level [7]. The pathways involved in astrocyte release of vasodilators are also likely to vary. For example, astrocyte P2X purinoreceptors have been suggested to contribute to PGE2 release at the capillary level [7]. Lastly, depending on the nature of the neuro-gliovascular unit at stake, other cell types such as endothelial cells are likely to contribute to NVC [81–84]. Future *in vivo* experiments monitoring Ca^{2+} activity in endfeet and its dependence to PLC activity, as well as its reliance on the nature of the neighboring vascular structure, will be important to test and refine our understanding of the mechanisms dictating NVC.

In line with recent translatome [29] and proteomics data [30–32], the spatial implementation of the model assumes that PGE2 signaling is restricted to the endfeet. Indeed, mGluR and molecules of the PGE2 pathway are enriched in endfeet compared to other astrocyte sub-cellular compartments. Our *in silico* experiments suggest that stimulating the astrocyte elsewhere than the endfoot compartment would trigger attenuated or no endfoot Ca^{2+} elevations and hardly any arteriole dilation. In these simulations of our model, Ca^{2+} and IP_3 could not diffuse quickly enough or in sufficient quantities from the stimulated compartments to the endfoot to trigger the same dilation as when the endfoot was stimulated. This result suggests that astrocyte-mediated NVC might occur locally, at the endfoot level. Interestingly, recent EM data support this view, as synapses have been observed in direct contact with endfeet [69]. As the number of synapses in contact with endfeet is likely to change depending on physiological conditions, we simulated the effect of the amount of glutamatergic input on blood vessel dilation. Our results suggest that an increased number of synapses contacting the endfoot would amplify the late-phase of NVC while a decrease in synaptic connectivity would impair NVC. Congruently, synapse loss and neurovascular uncoupling are observed in early stages of Alzheimer's disease (AD), which contributes to cognitive decline [5, 10]. The temporality of neuro-gliovascular dysfunction in AD at the subcellular level remains to be explored and should provide novel insights into AD pathogenesis. Overall, our results, in line with previous reports [20], challenge the classical view that opposes perivascular and perisynaptic processes as different entities and suggest that endfeet could be both, which would allow them to act as modulators of NVC at the sub-cellular level. A thorough investigation of the synaptic environment of endfeet will be critical to refine the view of endfeet as perisynaptic entities. The development of computer vision tools tailored to astrocytes will be critical to achieving this goal [85].

The model presented here is a generic model of astrocyte-dependent neurovascular coupling, based on omics data capturing the ribosomal RNA expression in endfeet [29], the interactome of aquaporin 4 [32], a water channel enriched in endfeet, as well as the endfoot proteome [30, 31]. These datasets shed light on proteins expressed in a population of astrocytic endfeet but do not allow to discriminate proteins expressed by different astrocytes or different endfeet. Notably, most of these datasets are enriched in endfeet neighboring capillaries and might thus poorly reflect the proteome of endfeet at the arteriolar interface. Given the growing literature on astrocyte diversity in health and disease [86–89] and the local translation of proteins in endfeet [29–31], it is tempting to speculate that endfeet may be heterogeneous and display different local proteomes depending on their biochemical and cellular environment. In particular, it seems likely that endfeet in contact with capillaries perform different functions than those in contact with arterioles [7]. Successful molecular dissection of endfoot functional heterogeneity and plasticity is thus a promising venue for future research and will be

instrumental in refining our understanding of the gliovascular unit and its diversity in health and disease.

In conclusion, our model proposes new interpretations of the role of astrocytes in NVC and suggests that the endfoot compartment, which enwraps blood vessels, could be a critical local mediator of NVC. Future research will be essential to characterize the inter-cellular and intra-cellular variability of these sub-cellular units in various physiological conditions and may provide cues for novel therapeutic strategies targeting NVC deficiencies.

Acknowledgments

The authors thank the teams of Martine Cohen-Salmon and Blanca Diaz-Castro for sharing omics datasets and providing critical insights into local expression in astrocyte endfeet, as well as Prof. Keith Murai for kindly sharing unpublished endfeet FIB-SEM datasets. The authors have no competing interests to declare that are relevant to the content of this article.

Data availability

The script that queries and aggregates the data from the four astrocyte omics studies used to model astrocyte-mediated NVC is available at https://gitlab.inria.fr/florian.dupeuble/endfeet_omics_analysis. The code of the model, implemented in Python, is available at https://gitlab.inria.fr/florian.dupeuble/astrovascular.

References

1. Drew PJ. Neurovascular coupling: motive unknown. Trends in Neurosciences. 2022 Nov;45(11):809-19. Available from: https://www.cell.com/trends/neurosciences/abstract/S0166-2236(22)00161-8. doi:10.1016/j.tins.2022.08.004.

2. Attwell D, Iadecola C. The neural basis of functional brain imaging signals. Trends in Neurosciences. 2002 Dec;25(12):621-5. Available from: https://www.cell.com/trends/neurosciences/abstract/S0166-2236(02)02264-6. doi:10.1016/S0166-2236(02)02264-6.

3. Zhu WM, Neuhaus A, Beard DJ, Sutherland BA, DeLuca GC. Neurovascular coupling mechanisms in health and neurovascular uncoupling in Alzheimer's disease. Brain. 2022 Jul;145(7):2276-92. Available from: https://doi.org/10.1093/brain/awac174. doi:10.1093/brain/awac174.

4. Iadecola C. The Neurovascular Unit Coming of Age: A Journey through Neurovascular Coupling in Health and Disease. Neuron. 2017 Sep;96(1):17-42. Available from: https://www.cell.com/neuron/abstract/S0896-6273(17)30652-9. doi:10.1016/j.neuron.2017.07.030.

5. Lourenço CF, Ledo A, Barbosa RM, Laranjinha J. Neurovascular uncoupling in the triple transgenic model of Alzheimer's disease: Impaired cerebral blood flow response to neuronal-derived nitric oxide signaling. Experimental Neurology. 2017

May;291:36-43. Available from: https://www.sciencedirect.com/science/article/pii/S0014488617300225. doi:10.1016/j.expneurol.2017.01.013.

6. Hosford PS, Gourine AV. What is the key mediator of the neurovascular coupling response? Neuroscience & Biobehavioral Reviews. 2019 Jan;96:174-81. Available from: https://www.sciencedirect.com/science/article/pii/S0149763418306158. doi:10.1016/j.neubiorev.2018.11.011.

7. Mishra A, Reynolds JP, Chen Y, Gourine AV, Rusakov DA, Attwell D. Astrocytes mediate neurovascular signaling to capillary pericytes but not to arterioles. Nature Neuroscience. 2016 Dec;19(12):1619-27. Available from: https://www-nature-com.insb.bib.cnrs.fr/articles/nn.4428. doi:10.1038/nn.4428.

8. Institoris A, Vandal M, Peringod G, Catalano C, Tran CH, Yu X, et al. Astrocytes amplify neurovascular coupling to sustained activation of neocortex in awake mice. Nature Communications. 2022 Dec;13(1):7872. Number: 1. Available from: https://www.nature.com/articles/s41467-022-35383-2. doi:10.1038/s41467-022-35383-2.

9. Drew PJ, Shih AY, Kleinfeld D. Fluctuating and sensory-induced vasodynamics in rodent cortex extend arteriole capacity. Proceedings of the National Academy of Sciences. 2011 May;108(20):8473-8. Available from: https://www.pnas.org/doi/full/10.1073/pnas.1100428108. doi:10.1073/pnas.1100428108.

10. Iadecola C. Neurovascular regulation in the normal brain and in Alzheimer's disease. Nature Reviews Neuroscience. 2004 May;5(5):347-60. Available from: https://www.nature.com/articles/nrn1387. doi:10.1038/nrn1387.

11. Mathiisen TM, Lehre KP, Danbolt NC, Ottersen OP. The perivascular astroglial sheath provides a complete covering of the brain microvessels: An electron microscopic 3D reconstruction. Glia. 2010;58(9):1094-103. _eprint: https://onlinelibrary.wiley.com/doi/pdf/10.1002/glia.20990. Available from: https://onlinelibrary.wiley.com/doi/abs/10.1002/glia.20990. doi:10.1002/glia.20990.

12. Attwell D, Buchan AM, Charpak S, Lauritzen M, MacVicar BA, Newman EA. Glial and neuronal control of brain blood flow. Nature. 2010 Nov;468(7321):232-43. Available from: https://www.nature.com/articles/nature09613. doi:10.1038/nature09613.

13. Del Franco AP, Chiang PP, Newman EA. Dilation of cortical capillaries is not related to astrocyte calcium signaling. Glia. 2022;70(3):508-21. _eprint: https://onlinelibrary.wiley.com/doi/pdf/10.1002/glia.24119. Available from: https://onlinelibrary.wiley.com/doi/abs/10.1002/glia.24119. doi:10.1002/glia.24119.

14. Tran CHT, Peringod G, Gordon GR. Astrocytes Integrate Behavioral State and Vascular Signals during Functional Hyperemia. Neuron. 2018 Oct. Available from: http://www.sciencedirect.com/science/article/pii/S089662731830847X. doi:10.1016/j.neuron.2018.09.045.

15. Vittani M, Herlo R, Wang X, Christensen MDB, Vo CT, Mishima T, et al. Cerebral blood flow is modulated by astrocytic cAMP elevation independently of IP3R2-mediated Ca2+ signaling in mice. Proceedings of the National Academy of Sciences. 2025 Jul;122(27):e2422069122. Available from: https://www.pnas.org/doi/10.1073/pnas.2422069122. doi:10.1073/pnas.2422069122.

16. Stobart JL, Ferrari KD, Barrett MJP, Glück C, Stobart MJ, Zuend M, et al. Cortical Circuit Activity Evokes Rapid Astrocyte Calcium Signals on a Similar Timescale to Neurons. Neuron. 2018 May;98(4):726-35.e4. Available from: http://www.sciencedirect.com/science/article/pii/S0896627318302848. doi:10.1016/j.neuron.2018.03.050.

17. Otsu Y, Couchman K, Lyons DG, Collot M, Agarwal A, Mallet JM, et al. Calcium dynamics in astrocyte processes during neurovascular coupling. Nature Neuroscience. 2015 Feb;18(2):210-8. Available from: http://www.nature.com/neuro/journal/v18/n2/full/nn.3906.html. doi:10.1038/nn.3906.

18. Bazargani N, Attwell D. Astrocyte calcium signaling: the third wave. Nature Neuroscience. 2016 Feb;19(2):182-9. doi:10.1038/nn.4201.

19. Kameyama T, Miyata M, Shiotani H, Adachi J, Kakuta S, Uchiyama Y, et al. Heterogeneity of perivascular astrocyte endfeet depending on vascular regions in the mouse brain. iScience. 2023 Sep:108010. Available from: https://linkinghub.elsevier.com/retrieve/pii/S2589004223020874. doi:10.1016/j.isci.2023.108010.

20. Cohen-salmon M, Guille N, Boulay AC. Development of perivascular astrocyte processes. Frontiers in Neuroscience. 2025 Jun;19. Available from: https://www.frontiersin.org/journals/neuroscience/articles/10.3389/fnins.2025.1585340/full. doi:10.3389/fnins.2025.1585340.

21. Huneau C, Benali H, Chabriat H. Investigating Human Neurovascular Coupling Using Functional Neuroimaging: A Critical Review of Dynamic Models. Frontiers in Neuroscience. 2015 Dec;9:467. Available from: https://hal.sorbonne-universite.fr/hal-01266115. doi:10.3389/fnins.2015.00467.

22. Bennett MR, Farnell L, Gibson WG. Origins of blood volume change due to glutamatergic synaptic activity at astrocytes abutting on arteriolar smooth muscle cells. Journal of Theoretical Biology. 2008 Jan;250(1):172-85. Available from: https://www.sciencedirect.com/science/article/pii/S0022519307004110. doi:10.1016/j.jtbi.2007.08.024.

23. Farr H, David T. Models of neurovascular coupling via potassium and EET signalling. Journal of Theoretical Biology. 2011 Oct;286:13-23. Available from: https://www.sciencedirect.com/science/article/pii/S002251931100350X. doi:10.1016/j.jtbi.2011.07.006.

24. Kenny A, Plank MJ, David T. The role of astrocytic calcium and TRPV4 channels in neurovascular coupling. Journal of Computational Neuroscience. 2018 Feb;44(1):97-114. Available from: https://doi.org/10.1007/s10827-017-0671-7. doi:10.1007/s10827-017-0671-7.

25. Dormanns K, van Disseldorp EMJ, Brown RG, David T. Neurovascular coupling and the influence of luminal agonists via the endothelium. Journal of Theoretical Biology. 2015 Jan;364:49-70. Available from: https://www.sciencedirect.com/science/article/pii/S0022519314004901. doi:10.1016/j.jtbi.2014.08.029.

26. Mathias EJ, Kenny A, Plank MJ, David T. Integrated models of neurovascular coupling and BOLD signals: Responses for varying neural activations. NeuroImage. 2018 Jul;174:69-86. Available from: https://www.sciencedirect.com/science/article/pii/S1053811918302052. doi:10.1016/j.neuroimage.2018.03.010.

27. Tesler F, Linne ML, Destexhe A. Modeling the relationship between neuronal activity and the BOLD signal: contributions from astrocyte calcium dynamics. Scientific Reports. 2023 Apr;13(1):6451. Number: 1. Available from: https://www.nature.com/articles/s41598-023-32618-0. doi:10.1038/s41598-023-32618-0.

28. Sten S, Podéus H, Sundqvist N, Elinder F, Engström M, Cedersund G. A quantitative model for human neurovascular coupling with translated mechanisms from animals. PLOS Computational Biology. 2023 Jan;19(1):e1010818. Available from: https://journals.plos.org/ploscompbiol/article?id=10.1371/journal.pcbi.1010818. doi:10.1371/journal.pcbi.1010818.

29. Boulay AC, Saubaméa B, Adam N, Chasseigneaux S, Mazaré N, Gilbert A, et al. Translation in astrocyte distal processes sets molecular heterogeneity at the gliovascular interface. Cell Discovery. 2017 Mar;3:17005. Available from: https://www.ncbi.nlm.nih.gov/pmc/articles/PMC5368712/. doi:10.1038/celldisc.2017.5.

30. Hill SA, Bravo-Ferrer I, Čiulkinytė A, Pérez Ramos N, Rossetti I, Colvin C, et al. Molecular profiling of brain endothelial cell to astrocyte endfoot communication in mouse and human. Nature Communications. 2025 Nov;16(1):9750. Available from: https://www.nature.com/articles/s41467-025-65487-4. doi:10.1038/s41467-025-65487-4.

31. Stokum JA, Shim B, Huang W, Kane M, Smith JA, Gerzanich V, et al. A large portion of the astrocyte proteome is dedicated to perivascular endfeet, including critical components of the electron transport chain. Journal of Cerebral Blood Flow & Metabolism. 2021 Oct;41(10):2546-60. Available from: https://doi.org/10.1177/0271678X211004182. doi:10.1177/0271678X211004182.

32. Soto JS, Jami-Alahmadi Y, Chacon J, Moye SL, Diaz-Castro B, Wohlschlegel JA, et al. Astrocyte–neuron subproteomes and obsessive–compulsive disorder mechanisms. Nature. 2023 Apr;616(7958):764-73. Number: 7958. Available from: https://www.nature.com/articles/s41586-023-05927-7. doi:10.1038/s41586-023-05927-7.

33. De Pittà M, Ben-Jacob E, Berry H. G Protein-Coupled Receptor-Mediated Calcium Signaling in Astrocytes. In: De Pittà M, Berry H, editors. Computational Glioscience. Springer Series in Computational Neuroscience. Cham: Springer International Publishing; 2019. p. 115-50.

34. Calvetti D, Prezioso J, Somersalo E. Estimating hemodynamic stimulus and blood vessel compliance from cerebral blood flow data. Journal of Theoretical

Biology. 2019 Jan;460:243-61. Available from: https://www.sciencedirect.com/science/article/pii/S0022519318304818. doi:10.1016/j.jtbi.2018.10.011.

35. Barrett MJP, Tawhai MH, Suresh V. Arteries dominate volume changes during brief functional hyperemia: Evidence from mathematical modelling. NeuroImage. 2012 Aug;62(1):482-92. Available from: https://www.sciencedirect.com/science/article/pii/S1053811912004934. doi:10.1016/j.neuroimage.2012.05.005.

36. Clements JD, Lester RAJ, Tong G, Jahr CE, Westbrook GL. The Time Course of Glutamate in the Synaptic Cleft. Science. 1992 Nov;258(5087):1498-501. Available from: https://www.science.org/doi/abs/10.1126/science.1359647. doi:10.1126/science.1359647.

37. Roxin A, Brunel N, Hansel D, Mongillo G, Vreeswijk Cv. On the Distribution of Firing Rates in Networks of Cortical Neurons. Journal of Neuroscience. 2011 Nov;31(45):16217-26. Available from: https://www.jneurosci.org/content/31/45/16217. doi:10.1523/JNEUROSCI.1677-11.2011.

38. Corrotte M, Chasserot-Golaz S, Huang P, Du G, Ktistakis NT, Frohman MA, et al. Dynamics and Function of Phospholipase D and Phosphatidic Acid During Phagocytosis. Traffic. 2006;7(3):365-77. _eprint: https://onlinelibrary.wiley.com/doi/pdf/10.1111/j.1600-0854.2006.00389.x. Available from: https://onlinelibrary.wiley.com/doi/abs/10.1111/j.1600-0854.2006.00389.x. doi:10.1111/j.1600-0854.2006.00389.x.

39. Martin TW. Formation of diacylglycerol by a phospholipase D-phosphatidate phosphatase pathway specific for phosphatidylcholine in endothelial cells. Biochimica et Biophysica Acta (BBA) - Lipids and Lipid Metabolism. 1988 Oct;962(3):282-96. Available from: https://www.sciencedirect.com/science/article/pii/0005276088902585. doi:10.1016/0005-2760(88)90258-5.

40. Rebecchi MJ, Pentyala SN. Structure, Function, and Control of Phosphoinositide-Specific Phospholipase C. Physiological Reviews. 2000 Jan;80(4):1291-335. Available from: https://journals.physiology.org/doi/full/10.1152/physrev.2000.80.4.1291. doi:10.1152/physrev.2000.80.4.1291.

41. Swinney DC, Mak AY, Barnett J, Ramesha CS. Differential Allosteric Regulation of Prostaglandin H Synthase 1 and 2 by Arachidonic Acid *. Journal of Biological Chemistry. 1997 May;272(19):12393-8. Available from: https://www.jbc.org/article/S0021-9258(18)40428-0/abstract. doi:10.1074/jbc.272.19.12393.

42. Park JY, Pillinger MH, Abramson SB. Prostaglandin E2 synthesis and secretion: The role of PGE2 synthases. Clinical Immunology. 2006 Jun;119(3):229-40. Available from: https://www.sciencedirect.com/science/article/pii/S1521661606000453. doi:10.1016/j.clim.2006.01.016.

43. Aretxabala X, García del Caño G, Barrondo S, López de Jesús M, González-Burguera I, Saumell-Esnaola M, et al. Endocannabinoid 2-Arachidonoylglycerol Synthesis and Metabolism at Neuronal Nuclear Matrix Fractions Derived from Adult Rat Brain Cortex. International Journal of Molecular Sciences. 2023 Jan;24(4):3165. Available from: https://www.mdpi.com/1422-0067/24/4/3165. doi:10.3390/ijms24043165.

44. Bisogno T, Howell F, Williams G, Minassi A, Cascio MG, Ligresti A, et al. Cloning of the first sn1-DAG lipases points to the spatial and temporal regulation of endocannabinoid signaling in the brain. The Journal of Cell Biology. 2003 Nov;163(3):463. Available from: https://pmc.ncbi.nlm.nih.gov/articles/PMC2173631/. doi:10.1083/jcb.200305129.

45. Savinainen JR, Saario SM, Laitinen JT. The serine hydrolases MAGL, ABHD6 and ABHD12 as guardians of 2-arachidonoylglycerol signalling through cannabinoid receptors. Acta Physiologica. 2012;204(2):267-76. _eprint: https://onlinelibrary.wiley.com/doi/pdf/10.1111/j.1748-1716.2011.02280.x. Available from: https://onlinelibrary.wiley.com/doi/abs/10.1111/j.1748-1716.2011.02280.x. doi:10.1111/j.1748-1716.2011.02280.x.

46. Siddiqi AR, Srajer GE, Leslie CC. Regulation of human PLD1 and PLD2 by calcium and protein kinase C. Biochimica et Biophysica Acta (BBA) - Molecular Cell Research. 2000 Jun;1497(1):103-14. Available from: https://www.sciencedirect.com/science/article/pii/S0167488900000495. doi:10.1016/S0167-4889(00)00049-5.

47. De Pittà MD, Goldberg M, Volman V, Berry H, Ben-Jacob E. Glutamate regulation of calcium and IP<Subscript>3</Subscript> oscillating and pulsating dynamics in astrocytes. Journal of Biological Physics. 2009 Oct;35(4):383-411. Available from: https://link.springer.com/article/10.1007/s10867-009-9155-y. doi:10.1007/s10867-009-9155-y.

48. Li YX, Rinzel J. Equations for InsP3 receptor-mediated [Ca2+]i oscillations derived from a detailed kinetic model: a Hodgkin-Huxley like formalism. J Theor Biol. 1994 Feb;166(4):461-73. Available from: http://dx.doi.org/1994.1041. doi:1994.1041.

49. Gustavsson L, Moehren G, Torres-Marquez ME, Benistant C, Rubin R, Hoek JB. The role of cytosolic Ca2+, protein kinase C, and protein kinase A in hormonal stimulation of phospholipase D in rat hepatocytes. Journal of Biological Chemistry. 1994 Jan;269(2):849-59. Available from: https://www.sciencedirect.com/science/article/pii/S0021925817421909. doi:10.1016/S0021-9258(17)42190-9.

50. Zhang L, Wang M, Bisogno T, Marzo VD, Alger BE. Endocannabinoids Generated by Ca2+ or by Metabotropic Glutamate Receptors Appear to Arise from Different Pools of Diacylglycerol Lipase. PLOS ONE. 2011 Jan;6(1):e16305. Available from: https://journals.plos.org/plosone/article?id=10.1371/journal.pone.0016305. doi:10.1371/journal.pone.0016305.

51. Leduc M, Breton B, Galés C, Gouill CL, Bouvier M, Chemtob S, et al. Functional Selectivity of Natural and Synthetic Prostaglandin EP4 Receptor

Ligands. Journal of Pharmacology and Experimental Therapeutics. 2009 Oct;331(1):297-307. Available from: https://jpet.aspetjournals.org/content/331/1/297. doi:10.1124/jpet.109.156398.

52. Mandeville JB, Marota JJA, Ayata C, Zaharchuk G, Moskowitz MA, Rosen BR, et al. Evidence of a Cerebrovascular Postarteriole Windkessel with Delayed Compliance. Journal of Cerebral Blood Flow & Metabolism. 1999 Jun;19(6):679-89. Available from: https://doi.org/10.1097/00004647-199906000-00012. doi:10.1097/00004647-199906000-00012.

53. Sheller JR, Mitchell D, Meyrick B, Oates J, Breyer R. EP2 receptor mediates bronchodilation by PGE2 in mice. Journal of Applied Physiology. 2000 Jun;88(6):2214-8. Available from: https://journals.physiology.org/doi/full/10.1152/jappl.2000.88.6.2214. doi:10.1152/jappl.2000.88.6.2214.

54. Davis RJ, Murdoch CE, Ali M, Purbrick S, Ravid R, Baxter GS, et al. EP4 prostanoid receptor-mediated vasodilatation of human middle cerebral arteries. British Journal of Pharmacology. 2004;141(4):580-5. _eprint: https://bpspubs.onlinelibrary.wiley.com/doi/pdf/10.1038/sj.bjp.0705645. Available from: https://onlinelibrary.wiley.com/doi/abs/10.1038/sj.bjp.0705645. doi:10.1038/sj.bjp.0705645.

55. Vanlandewijck M, He L, Mäe MA, Andrae J, Ando K, Del Gaudio F, et al. A molecular atlas of cell types and zonation in the brain vasculature. Nature. 2018 Feb;554(7693):475-80. Available from: https://www.nature.com/articles/nature25739. doi:10.1038/nature25739.

56. He L, Vanlandewijck M, Mäe MA, Andrae J, Ando K, Del Gaudio F, et al. Single-cell RNA sequencing of mouse brain and lung vascular and vessel-associated cell types. Scientific Data. 2018 Aug;5(1):180160. Available from: https://www.nature.com/articles/sdata2018160. doi:10.1038/sdata.2018.160.

57. Regan JW. EP2 and EP4 prostanoid receptor signaling. Life Sciences. 2003 Dec;74(2):143-53. Available from: https://www.sciencedirect.com/science/article/pii/S002432050300907X. doi:10.1016/j.lfs.2003.09.031.

58. Aslam M, Härtel FV, Arshad M, Gündüz D, Abdallah Y, Sauer H, et al. cAMP/PKA antagonizes thrombin-induced inactivation of endothelial myosin light chain phosphatase: role of CPI-17. Cardiovascular Research. 2010 Jul;87(2):375-84. Available from: https://doi.org/10.1093/cvr/cvq065. doi:10.1093/cvr/cvq065.

59. Yang JX, Lin Y. The action of PKA on smooth muscle myosin phosphorylation. Life Sciences. 2005 Oct;77(21):2669-75. Available from: https://www.sciencedirect.com/science/article/pii/S0024320505005205. doi:10.1016/j.lfs.2005.04.026.

60. Hofer AM. Interactions Between Calcium and cAMP Signaling. Current Medicinal Chemistry. 2012 Dec;19(34):5768-73. Available from: https://www.benthamdirect.com/content/journals/cmc/10.2174/092986712804143286. doi:10.2174/092986712804143286.

61. Eymard R, Gallouët T, Herbin R. Finite volume methods. In: Handbook of Numerical Analysis. vol. 7. Elsevier; 2000. p. 713-1018. Available from: https://www.sciencedirect.com/science/chapter/handbook/abs/pii/S1570865900070058. doi:10.1016/S1570-8659(00)07005-8.

62. Covelo A, Badoual A, Denizot A. Reinforcing Interdisciplinary Collaborations to Unravel the Astrocyte "Calcium Code". Journal of Molecular Neuroscience. 2022 May. Available from: https://doi.org/10.1007/s12031-022-02006-w. doi:10.1007/s12031-022-02006-w.

63. Denizot A, Castillo MFV, Puchenkov P, Calì C, De Schutter E. The Ultrastructural Properties of the Endoplasmic Reticulum Govern Microdomain Signaling in Perisynaptic Astrocytic Processes. Glia. 2026;74(2):e70091. _eprint: https://onlinelibrary.wiley.com/doi/pdf/10.1002/glia.70091. Available from: https://onlinelibrary.wiley.com/doi/abs/10.1002/glia.70091. doi:10.1002/glia.70091.

64. Calì C, Baghabra J, Boges DJ, Holst GR, Kreshuk A, Hamprecht FA, et al. Three-dimensional immersive virtual reality for studying cellular compartments in 3D models from EM preparations of neural tissues. Journal of Comparative Neurology. 2016 Jan;524(1):23-38. Available from: v. doi:10.1002/cne.23852.

65. Baldwin KT, Murai KK, Khakh BS. Astrocyte morphology. Trends in Cell Biology. 2023 Oct. Available from: https://www.sciencedirect.com/science/article/pii/S0962892423002040. doi:10.1016/j.tcb.2023.09.006.

66. Lourenço CF, Santos RM, Barbosa RM, Cadenas E, Radi R, Laranjinha J. Neurovascular coupling in hippocampus is mediated via diffusion by neuronal-derived nitric oxide. Free Radical Biology and Medicine. 2014 Aug;73:421-9. Available from: https://www.sciencedirect.com/science/article/pii/S0891584914002378. doi:10.1016/j.freeradbiomed.2014.05.021.

67. O'Gallagher K, Puledda F, O'Daly O, Ryan M, Dancy L, Chowienczyk PJ, et al. Neuronal nitric oxide synthase regulates regional brain perfusion in healthy humans. Cardiovascular Research. 2022 Apr;118(5):1321-9. Available from: https://doi.org/10.1093/cvr/cvab155. doi:10.1093/cvr/cvab155.

68. Yu X, Taylor AMW, Nagai J, Golshani P, Evans CJ, Coppola G, et al. Reducing Astrocyte Calcium Signaling In Vivo Alters Striatal Microcircuits and Causes Repetitive Behavior. Neuron. 2018 Sep;99(6):1170-87.e9. Available from: https://www.cell.com/neuron/abstract/S0896-6273(18)30688-3. doi:10.1016/j.neuron.2018.08.015.

69. Aten S, Kiyoshi CM, Arzola EP, Patterson JA, Taylor AT, Du Y, et al. Ultrastructural view of astrocyte arborization, astrocyte-astrocyte and astrocyte-synapse contacts, intracellular vesicle-like structures, and mitochondrial network. Progress in Neurobiology. 2022 Jun;213:102264. Available from: g. doi:10.1016/j.pneurobio.2022.102264.

70. Williamson JR, Cooper RH, Joseph SK, Thomas AP. Inositol trisphosphate and diacylglycerol as intracellular second messengers in liver. American Journal of Physiology-Cell Physiology. 1985 Mar;248(3):C203-16. Available from: https://journals.physiology.org/doi/abs/10.1152/ajpcell.1985.248.3.c203. doi:10.1152/ajpcell.1985.248.3.C203.

71. Allbritton NL, Meyer T, Stryer L. Range of messenger action of calcium ion and inositol 1,4,5-trisphosphate. Science (New York, NY). 1992 Dec;258(5089):1812-5.

72. Benoit L, Hristovska I, Liaudet N, Jouneau PH, Fertin A, de Ceglia R, et al. Astrocytes functionally integrate multiple synapses via specialized leaflet domains. Cell. 2025 Sep. Available from: https://www.sciencedirect.com/science/article/pii/S0092867425010281. doi:10.1016/j.cell.2025.08.036.

73. Takano T, Tian GF, Peng W, Lou N, Libionka W, Han X, et al. Astrocyte-mediated control of cerebral blood flow. Nature Neuroscience. 2006 Feb;9(2):260-7. doi:10.1038/nn1623.

74. Zonta M, Angulo MC, Gobbo S, Rosengarten B, Hossmann KA, Pozzan T, et al. Neuron-to-astrocyte signaling is central to the dynamic control of brain microcirculation. Nature Neuroscience. 2002 Nov;6(1):nn980. Available from: https://www.nature.com/articles/nn980. doi:10.1038/nn980.

75. Filosa JA, Bonev AD, Nelson MT. Calcium dynamics in cortical astrocytes and arterioles during neurovascular coupling. Circulation Research. 2004 Nov;95(10):e73-81. doi:10.1161/01.RES.0000148636.60732.2e.

76. Lind BL, Volterra A. Fast 3D imaging in the auditory cortex of awake mice reveals that astrocytes control neurovascular coupling responses locally at arteriole-capillary junctions. bioRxiv; 2025. Pages: 2024.06.28.601145 Section: New Results. Available from: https://www.biorxiv.org/content/10.1101/2024.06.28.601145v2. doi:10.1101/2024.06.28.601145.

77. Lourenço CF, Laranjinha J. Nitric Oxide Pathways in Neurovascular Coupling Under Normal and Stress Conditions in the Brain: Strategies to Rescue Aberrant Coupling and Improve Cerebral Blood Flow. Frontiers in Physiology. 2021 Oct;12. Available from: https://www.frontiersin.org/journals/physiology/articles/10.3389/fphys.2021.729201/full. doi:10.3389/fphys.2021.729201.

78. Lourenço CF, Ferreira NR, Santos RM, Lukacova N, Barbosa RM, Laranjinha J. The pattern of glutamate-induced nitric oxide dynamics *in vivo* and its correlation with nNOS expression in rat hippocampus, cerebral cortex and striatum. Brain Research. 2014 Mar;1554:1-11. Available from: https://www.sciencedirect.com/science/article/pii/S0006899314000833. doi:10.1016/j.brainres.2014.01.030.

79. Petzold GC, Albeanu DF, Sato TF, Murthy VN. Coupling of neural activity to blood flow in olfactory glomeruli is mediated by astrocytic pathways. Neuron. 2008 Jun;58(6):897-910. doi:10.1016/j.neuron.2008.04.029.

80. Zhang D, Ruan J, Peng S, Li J, Hu X, Zhang Y, et al. Synaptic-like transmission between neural axons and arteriolar smooth muscle cells drives cerebral neurovascular coupling. Nature Neuroscience. 2024 Feb;27(2):232-48. Available from: https://www.nature.com/articles/s41593-023-01515-0. doi:10.1038/s41593-023-01515-0.

81. Chow BW, Nuñez V, Kaplan L, Granger AJ, Bistrong K, Zucker HL, et al. Caveolae in CNS arterioles mediate neurovascular coupling. Nature. 2020 Mar;579(7797):106-10. Available from: https://www.nature.com/articles/s41586-020-2026-1. doi:10.1038/s41586-020-2026-1.

82. Lu L, Hogan-Cann AD, Globa AK, Lu P, Nagy JI, Bamji SX, et al. Astrocytes drive cortical vasodilatory signaling by activating endothelial NMDA receptors. Journal of Cerebral Blood Flow & Metabolism. 2019 Mar;39(3):481-96. Available from: https://doi.org/10.1177/0271678X17734100. doi:10.1177/0271678X17734100.

83. Krolak T, Kaplan L, Navas K, Chen L, Birmingham A, Ryvkin D, et al. Brain endothelial gap junction coupling enables rapid vasodilation propagation during neurovascular coupling. Cell. 2025 Jul;0(0). Available from: https://www.cell.com/cell/abstract/S0092-8674(25)00732-9. doi:10.1016/j.cell.2025.06.030.

84. Thakore P, Alvarado MG, Ali S, Mughal A, Pires PW, Yamasaki E, et al. Brain endothelial cell TRPA1 channels initiate neurovascular coupling. eLife. 2021 Feb;10:e63040. Available from: https://doi.org/10.7554/eLife.63040. doi:10.7554/eLife.63040.

85. Syed TA, Youssef M, Schober AL, Kubota Y, Murai KK, Salmon CK. Beyond neurons: computer vision methods for analysis of morphologically complex astrocytes. Frontiers in Computer Science. 2024 Sep;6. Available from: https://www.frontiersin.org/journals/computer-science/articles/10.3389/fcomp.2024.1156204/full. doi:10.3389/fcomp.2024.1156204.

86. Baldwin KT. Molecular diversity of astrocytes. Science. 2022 Nov;378(6619):475-6. Available from: https://www.science.org/doi/full/10.1126/science.ade9249. doi:10.1126/science.ade9249.

87. Khakh BS, Sofroniew MV. Diversity of astrocyte functions and phenotypes in neural circuits. Nature Neuroscience. 2015 Jul;18(7):942-52. doi:10.1038/nn.4043.

88. Khakh BS, Deneen B. The Emerging Nature of Astrocyte Diversity. Annual Review of Neuroscience. 2019;42(1):187-207. _eprint: https://doi.org/10.1146/annurev-neuro-070918-050443. Available from: https://doi.org/10.1146/annurev-neuro-070918-050443. doi:10.1146/annurev-neuro-070918-050443.

89. Clayton BLL, Liddelow SA. Heterogeneity of Astrocyte Reactivity. Annual Review of Neuroscience. 2025 Jul;48(Volume 48, 2025):231-49. Available from: https://www.annualreviews.org/content/journals/10.1146/annurev-neuro-112723-031738. doi:10.1146/annurev-neuro-112723-031738.

Supporting Information

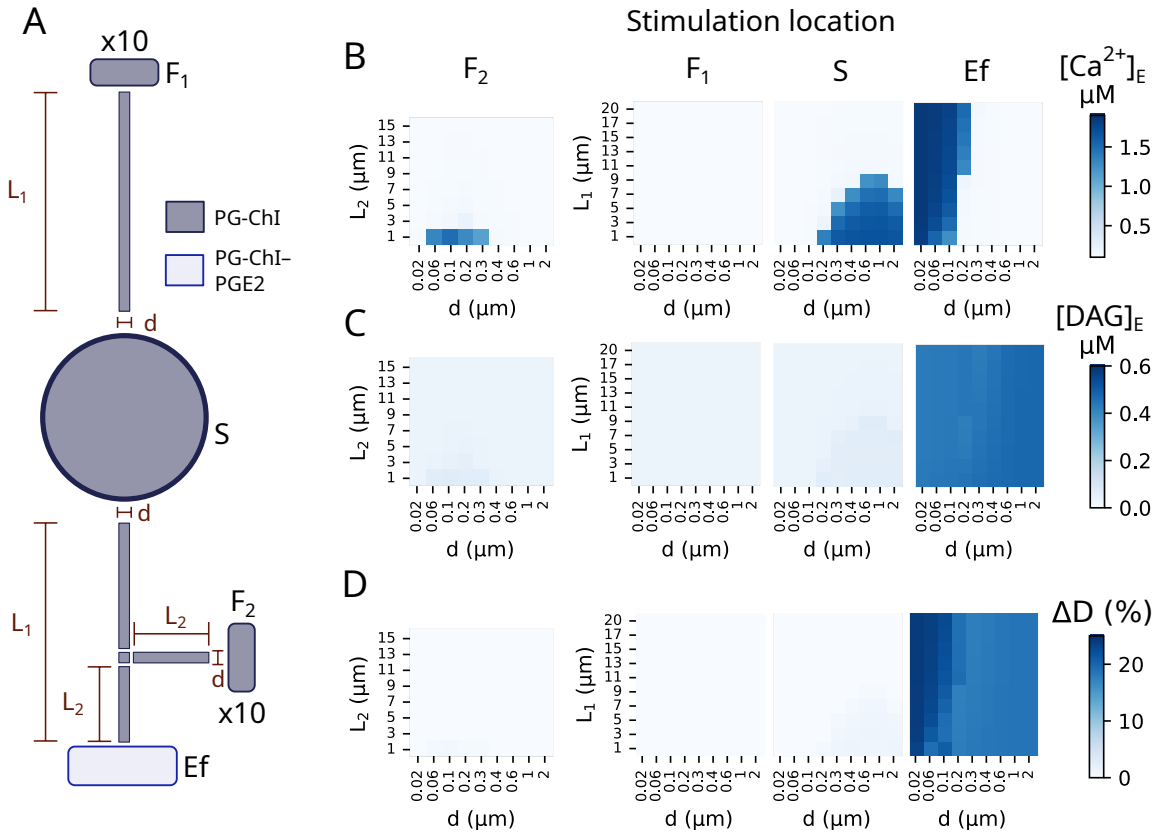

Figure S1: **Activation of leaflet domains does not trigger NVC in the model, confirming that astrocyte PGE2-mediated vasodilation only happens when neuronal stimulation occurs at the endfoot level.** (A) Schematic representation of the simplified astrocyte geometry in the spatial model. In contrast to figure 6 of the main text, F_1 and F_2 correspond to leaflet domains which contain 10 leaflets each (see Methods and supplementary text S2 for details).
Panel (B-D) show heatmaps of the peak endfoot Ca^{2+} concentration ($[Ca^{2+}]_E$, B), the maximal endfoot DAG concentration ($[DAG]_E$, C), and the maximal relative arteriole dilation (ΔD, D), at different stimulation locations: leaflet domains (F2, left, and F1, middle left), soma (S, middle right), and endfoot (Ef, right)). In *in silico* experiments, L_1 was set to 20 μm when varying L_2. L_2 was set to $L_1/2$ when varying L_1.

Table S1: **Parameter values of the astrocyte Ca^{2+} signaling model.** It corresponds to the G-ChI model [1, 2].

Parameter	Description	Value	Unit	Reference
ER-related variables				
ν_{ER}	Maximal rate of SERCA uptake	0.83	$\mu M.s^{-1}$	[2]
K_{ER}	SERCA Ca^{2+} affinity	0.124	μM	[2]
a_2	IP_3R binding rate for Ca^{2+} inhibition	0.18	s^{-1}	[2]
c_0	Total free Ca^{2+} concentration	2.8	μM	[2]
c_1	ER/cytosol volume ratio	0.16	-	[2]
r_c	Maximal Ca^{2+} release rate through open IP_3R	9.4	s^{-1}	-
r_L	Ca^{2+} leak rate	0.13	s^{-1}	[2]
d_1	IP_3 binding affinity	0.21	μM	-
d_2	IP_3R Ca^{2+} inactivation dissociation constant	0.9	μM	[2]
d_3	IP_3 binding affinity (with Ca^{2+} inactivation)	0.07	μM	[2]
d_5	Activating Ca^{2+} binding activity	0.4	μM	-
IP_3 dynamics				
ν_{3K}	Maximal rate of IP_3 degradation by IP3-3K	0.85	$\mu M.s^{-1}$	[1]
K_3	IP_3 affinity of IP_3-3K	0.19	μM	-
K_D	Ca^{2+} affinity to IP_3-3K	0.71	μM	[2]
r_{5P}	Rate of IP_3 degradation by IP-5P	0.29	s^{-1}	-
ν_β	Maximal rate of IP_3 and DAG production by PLCβ	0.97	$\mu M.s^{-1}$	[1]
ν_δ	Maximal rate of IP_3 and DAG production by PLCδ	0.085	$\mu M.s^{-1}$	[1]
K_δ	Ca^{2+} affinity of PLCδ	0.38	μM	[1]
κ_d	Inhibiting IP_3 affinity of PLCδ	0.8	μM	[1]
DAG dynamics				
K_{DC}	DAGK affinity for Ca^{2+}	1.3	μM	-
K_{DD}	DAGK affinity for DAG	0.11	μM	[1]
ν_d	Rate of degradation by DAGK	0.7	$\mu M.s^{-1}$	[1]
cPKC dynamics				
ν_{kd}	Rate of cPKC production	4.4	$\mu M.s^{-1}$	-
ω_{kd}	Rate of cPKC deactivation	1.8	s^{-1}	-
ν_k	Rate of receptor phosphorylation by cPKC	3.7	$\mu M^{-1}s^{-1}$	-
K_{KC}	Ca^{2+} affinity of PKC	0.22	μM	-
mGluR dynamics				
ω_n	Rate of mGluR receptor de-activation	1.7	s^{-1}	[1]
o_n	Rate of agonist-mediated mGluR receptor activation	0.3	$\mu M^{-1}s^{-1}$	[1]
Glutamate dynamics				
τ_G	Glutamate degradation rate	0.003	s^{-1}	[3]
ν_G	Maximal neuronal glutamate release	600.0	$\mu M.s^{-1}$	[3]

Table S2: **Parameter values of the vasculature model.** The model is an extension of the three-compartment Windkessel model, parameter values were taken from [4].

Parameter	Description	value	Units	Reference
Vasodilators effects				
O_c	Maximal cAMP effect on relative arteriole dilation	3.8	-	-
K_{cAMP}	Half cAMP activation concentration	0.65	μM	-
n_c	cAMP effect on relative arteriole dilation Hill coefficient	2	-	-
O_n	Maximal NO effect on arteriole dilation	0.38	-	-
Stiffness coefficients				
K_a	Arteriole stiffness coefficient	5.0	-	-
K_c	Capillaries stiffness coefficient	2.0	-	-
K_v	Venules stiffness coefficient	2.0	-	-
Viscoelastic coefficients				
$k_{vis,a}$	Arteriole viscoelastic parameter	1.5	-	-
$k_{vis,c}$	Capillaries viscoelastic parameter	1.5	-	-
$k_{vis,v}$	Venules viscoelastic parameter	1.5	-	-
Pressure on blood vessels				
$p_{a,0}$	Pressure at the arteriole entry point	1.0	-	[4]
$p_{c,0}$	Pressure at the capillaries entry point	0.26	-	[4]
$p_{v,0}$	Pressure at the venules entry point	0.18	-	[4]
Initial blood vessels resistance				
$R_{a,0}$	Initial arterioles resistance	0.74	-	[4]
$R_{c,0}$	Initial capillaries resistance	0.08	-	[4]
$R_{v,0}$	Initial venules resistance	0.18	-	[4]
Initial blood vessels volumes				
$V_{a,0}$	Initial relative arteriole volume	0.29	-	[4]
$V_{c,0}$	Initial relative capillaries volume	0.44	-	[4]
$V_{v,0}$	Initial relative venules volume	0.27	-	[4]

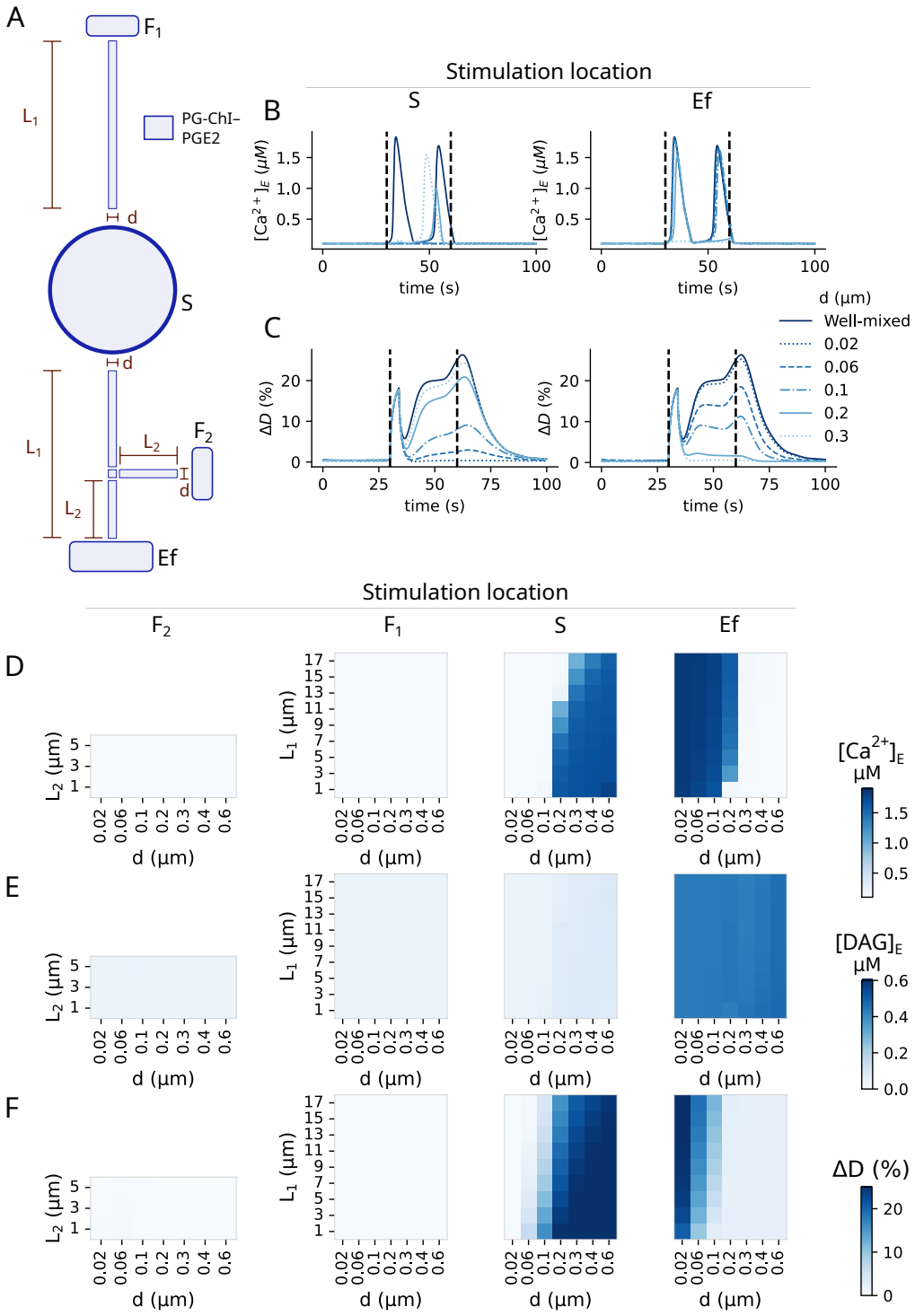

Figure S2: **Simulations of the spatial model suggest that astrocyte PGE2-mediated vasodilation can occur when neuronal stimulation occurs at the endfoot or at the somatic level when all compartments express molecules of the PGE2 pathway.** (A) Schematic representation of the simplified astrocyte geometry in the spatial model. Representative endfoot Ca^{2+} concentration (B) and ΔD (C) traces depending on branch diameter d in simulations, where either the soma (S, left), or the endfoot (Ef, right) was stimulated, $L_1 = 11$ μm and $L_2 = L_1/2$. Black vertical dashed lines delimit the neuronal stimulation period. Heatmaps show the peak concentration in the endfoot of Ca^{2+} concentration ($[Ca^{2+}]_E$, D), the maximal endfoot DAG concentration ($[DAG]_E$, E), and the maximum relative arteriole dilation (ΔD, F), at different stimulation locations: leaflets (F2, left, and F1, middle left), soma (S, middle right), and endfoot (Ef, right).

Supplementary materials S1

G-ChI model

The G-ChI model [1, 2] describes the dynamics of astrocyte calcium concentration $[Ca^{2+}]$, IP_3 concentration $[IP_3]$, DAG concentration $[DAG]$, cPKC concentration $[cPKC]$, the proportion of activated astrocyte mGluR receptors Γ and the IP_3R2 opening probability h, as follows:

$$\frac{d[Ca^{2+}]}{dt} = J_{chan} + J_{leak} - J_{pump} \tag{1}$$

$$\frac{d\Gamma}{dt} = o_n \cdot [G] \cdot (1 - \Gamma) - \omega_n \cdot \left(1 + \frac{\nu_k \cdot [cPKC]}{\omega_n}\right) \Gamma \tag{2}$$

$$\frac{d[IP_3]}{dt} = J_{PLC\beta} + J_{PLC\delta} - J_{phos} - J_{dephos} \tag{3}$$

$$\frac{dh}{dt} = a_2 \Big(d_2 \cdot \frac{[IP_3] + d_1}{[IP_3] + d_3} (1 - h) - [Ca^{2+}] \cdot h \Big) \tag{4}$$

$$\frac{d[DAG]}{dt} = J_{PLC\beta} + J_{PLC\delta} - J_{KP} - J_D - J_A \tag{5}$$

$$\frac{d[cPKC]}{dt} = J_{KP} - J_{KD} \tag{6}$$

where J_{chan} is the Ca^{2+} flux from the ER to the cytosol through open IP_3R channels, J_{leak} is the Ca^{2+} leak from the ER to the cytosol, and J_{pump} is the Ca^{2+} flux from the cytosol to the ER mediated by the Sarco-Endoplasmic Reticulum Ca^{2+} -ATPase (SERCA) pump. J_{phos} and J_{dephos} are the IP_3 phosphorylation and dephosphorylation rates, respectively. Parameter values of the G-ChI model as implemented here are depicted in Table S1. The fluxes scheme is depicted in figure S3.

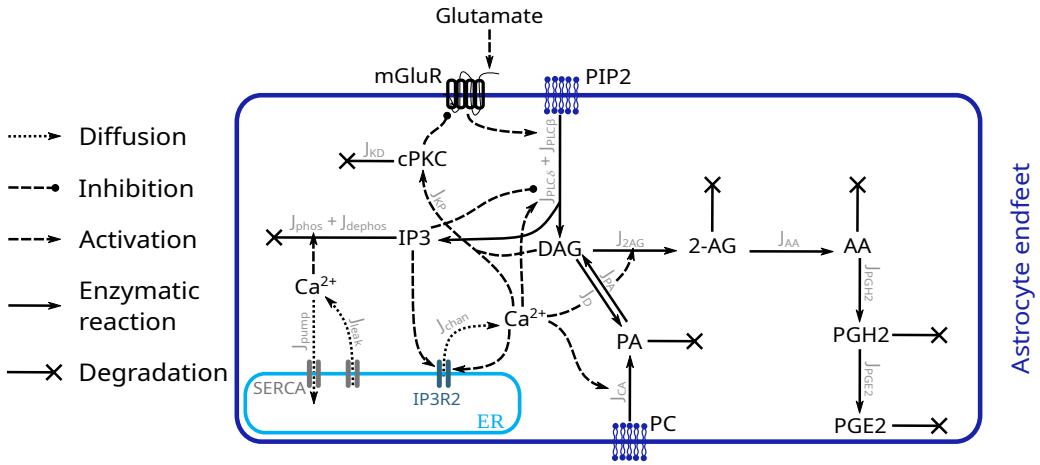

Figure S3: **Reaction scheme of the neurovascular coupling model illustrating the simulated fluxes.**

$$
\begin{aligned}
J_{chan} &= r_c \cdot \left(\frac{[IP_3]}{[IP_3]+d_1} \cdot \frac{[Ca^{2+}]}{[Ca^{2+}]+d_5} \cdot h \right)^3 \cdot \Big(c_0 - (1+c_1)[Ca^{2+}] \Big) \\
J_{leak} &= r_L (c_0 - (1+c_1)[Ca^{2+}]) \\
J_{pump} &= \nu_{ER} \cdot \frac{[Ca^{2+}]^2}{[Ca^{2+}]^2 + K_{ER}^2} \\
J_{PLC\delta} &= \nu_\delta \cdot \left(1 - \frac{[IP_3]}{[IP_3]+\kappa_d} \right) \cdot \frac{[Ca^{2+}]^2}{[Ca^{2+}]^2 + K_\delta^2} \\
J_{PLC\beta} &= \nu_\beta \Gamma \\
J_{phos} &= \nu_{3K} \cdot \frac{[Ca^{2+}]^4}{[Ca^{2+}]^4 + K_D^4} \cdot \frac{[IP_3]}{[IP_3]+K_3} \\
J_{dephos} &= r_{5P} \cdot [IP_3] \\
J_{KP} &= \nu_{kd} \cdot [DAG] \cdot \frac{[Ca^{2+}]}{[Ca^{2+}]+K_{KC}} \\
J_{KD} &= \omega_{kd} \cdot [cPKC] \\
J_D &= \nu_d \cdot \frac{[Ca^{2+}]^2}{[Ca^{2+}]^2 + K_{DC}^2} \cdot \frac{[DAG]^2}{[DAG]^2 + K_{DD}^2} \\
J_A &= \frac{[DAG]}{\tau_{DAG}}
\end{aligned}
$$

Supplementary materials S2

Diffusion inside branches

Branches are modeled as aligned identical cylinders, of length Δx and radius $d/2$, connected by their bases of diameter d and area $S_b = \pi \frac{d^2}{4}$. Noting n_i and C_i the molar quantity and the molar concentration in the i compartment of a branch, connected to the $i+1$ and $i-1$ compartments, the rate of change of the molar amount in compartment i is the net flux exchanged with the neighboring

compartments:

$$\frac{dn_i}{dt} = \Phi_{i-1} - \Phi_{i+1} = -D_C S_b \frac{C_i - C_{i-1}}{\Delta x} + D_C S_b \frac{C_{i+1} - C_i}{\Delta x} = D_C S_b \frac{C_{i-1} + C_{i+1} - 2C_i}{\Delta x}$$

Thus,

$$\frac{dC_i}{dt} = \frac{D_C S_b}{V_i} \frac{C_{i-1} + C_{i+1} - 2C_i}{\Delta x} \tag{7}$$

As $V_i = S_b \Delta x$, equation (7) becomes

$$\frac{dC_i}{dt} = D_C \frac{C_{i-1} + C_{i+1} - 2C_i}{(\Delta x)^2} \tag{8}$$

Diffusion between a branch and another compartment

The effective diffusion distance between the two compartments is approximated as the distance between their centers, i.e. $\frac{\Delta x}{2} + \frac{L}{2}$, with L the length of a large compartment (soma, endfoot, or leaflets) noted k. The flux between k and the connected cylinder of a branch is

$$\Phi_k = -D_C S_b \frac{C_k - C_i}{\frac{\Delta x}{2} + \frac{L}{2}} \tag{9}$$

The concentration of the diffusing molecule inside the ith cylinder thus becomes:

$$\frac{dC_i}{dt} = \Phi_i - \Phi_k = -D_C \frac{C_i - C_{i-1}}{(\Delta x)^2} + D_C S_b \frac{C_k - C_i}{V_i(\frac{\Delta x}{2} + \frac{L}{2})} \tag{10}$$

And the concentration inside the large k compartment is

$$\frac{dC_k}{dt} = \Phi_k + \Phi_{other} = -D_C S_b \frac{C_k - C_i}{V_k(\frac{\Delta x}{2} + \frac{L}{2})} + \Phi_{other} \tag{11}$$

where Φ_{other} corresponds to the flux between k and another compartment, other than i, which shape is the same as Φ_k or vanishes when k is connected to i only.

Connecting several leaflets to a compartment

To test the impact of stimulating multiple leaflets without drastically increasing the number of branches and thus minimizing the computational cost of the simulations, we considered simulating connected leaflets as a single leaflet with higher activity. Below, we demonstrate how n leaflets and their branches (referred to as the full version) can be approximated as a single leaflet with different geometrical parameters (referred to as the reduced version).

Trajectories of the diffusing variables of the PG-ChI-PGE2 model, in all compartments outside the n leaflets, should remain identical in the full and reduced models. The n leaflets and connected branches being only coupled with one compartment k, the condition is: $\forall t \in R^+$, $\frac{\partial C_k}{\partial t}$ is the same in the full version and in the reduced version of the model.
We note B the branches of the reduced compartments, b the branches before reduction, P_i the cylinders of B, p_i the cylinders of b. We want:

$$\begin{aligned} \frac{\partial C_k}{\partial t} &= \frac{n.J_{p_i}}{V_k} = \frac{J_{P_i}}{V_k} \\ \Leftrightarrow n.J_{p_i} &= J_{P_i} \\ \Leftrightarrow nD_C S_p \frac{C_{p_i} - C_k}{\Delta x_p} &= D_C S_P \frac{C_{P_i} - C_k}{\Delta x_P} \end{aligned}$$

By choosing $\Delta x_P = \Delta x_p$, and $S_P = nS_p$, the expression becomes:

$$C_{p_i} = C_{P_i} \tag{12}$$

For equation (12) to be true, it must be so at the initial state (initial conditions are thus set this way), and the following must be true:

$$\begin{aligned} &\frac{\partial C_{p_i}}{\partial t} = \frac{\partial C_{P_i}}{\partial t} \\ &\Rightarrow -\frac{D_C S_p}{V_p}\frac{C_{p_i} - C_k}{\frac{\Delta x_p}{2} + \frac{L}{2}} - \frac{D_C S_p}{V_p}\frac{C_{p_i} - C_{p_{i-1}}}{\Delta x_p} = -\frac{D_C S_P}{V_P}\frac{C_{P_i} - C_k}{\frac{\Delta x_P}{2} + \frac{L}{2}} - \frac{D_C S_P}{V_P}\frac{C_{P_i} - C_{P_{i-1}}}{\Delta x_P} \end{aligned} \tag{13}$$

Since $S_P = nS_p$, and $\Delta x_p = \Delta x_P$, $V_P = nV_p$, equation (13) becomes:

$$-(C_{p_i} - C_k) - (C_{p_i} - C_{p_{i-1}}) = -(C_{P_i} - C_k) - (C_{P_i} - C_{P_{i-1}})$$

Supposing equation (12) is true, we arrive at the following condition: $C_{p_{i-1}} = C_{P_{i-1}}$. By descending along the branch, we arrive at a last condition, where the exchange between leaflets and the connected branch must be the same in the full (compartment P_0) and reduced (compartments p_0) versions of the model. In other words, we want:

$$\begin{aligned} &\frac{\partial C_{P_0}}{\partial t} = \frac{\partial C_{p_0}}{\partial t} \\ &\Rightarrow -\frac{D_C S_P}{V_{P_0}}\frac{C_{P_0} - C_{p_1}}{\Delta x_p} = -\frac{D_C S_p}{V_{p_0}}\frac{C_{p_0} - C_{p_1}}{\Delta x_p} \end{aligned}$$

because $S_P = nS_p$, $C_{p_1} = C_{P_1}$ by recurrence, choosing $V_{P_0} = nV_{p_0}$, and the initial state $C_{p_0} = C_{P_0}$, we get $C_{P_0} = C_{p_0}$.

Connecting several leaflets to a branch

The demonstration from the previous section remains valid when connecting n branches b_1 to another branch b_2, provided that the connection occurs through a single subcompartment M of b_2. However, the geometry parameters of M must be defined carefully to ensure a consistent representation of the exchange surfaces. Indeed, when M corresponds to the soma, it is reasonable to consider that its surface is superior to nS_p. This assumption may no longer hold when M represents a portion of a branch. First, if M was modeled as a simple cylinder, the base of branch $b1$ could only contact M along a line, which would not provide any exchange surface for the modeled diffusion process. To overcome this problem, we define M as a composite geometry whose base consists of a half-disk of radius r, which is equal to the radius of b_2, attached to a rectangle of length $2r$ and width r. Therefore, the diffusion interface in b_2 remains unchanged. We denote by L_M the length of M. The leaflets are assumed to exchange molecules through the face F, defined by the rectangle base of length $2r$ and the length L_M. Branching n leaflets to M is only possible if the area of F is superior to the area of n branch bases, $2rL_M \geq n\pi r^2 \Leftrightarrow L_M \geq n\frac{\pi}{2}r$. We choose $L_M = 2nr$. Then, M volume is $V_M = 2nr.2r.r + \frac{1}{2}\pi r^2.2nr = nr^3(4+\pi)$

References

[1] De Pittà M, Ben-Jacob E, Berry H. G Protein-Coupled Receptor-Mediated Calcium Signaling in Astrocytes. In: De Pittà M, Berry H, editors. Computational Glioscience. Springer Series in Computational Neuroscience. Springer International Publishing; 2019. p. 115-50. Available from: `https://doi.org/10.1007/978-3-030-00817-8_5`. doi:10.1007/978-3-030-00817-8_5.

[2] De Pittà M, Goldberg M, Volman V, Berry H, Ben-Jacob E. Glutamate regulation of calcium and IP3 oscillating and pulsating dynamics in astrocytes. Journal of Biological Physics. 2009;35(4):383-411. Available from: `https://doi.org/10.1007/s10867-009-9155-y`. doi:10.1007/s10867-009-9155-y.

[3] Clements JD, Lester RAJ, Tong G, Jahr CE, Westbrook GL. The Time Course of Glutamate in the Synaptic Cleft. Science. 1992;258(5087):1498-501. Available from: https://www.science.org/doi/abs/10.1126/science.1359647. doi:10.1126/science.1359647.

[4] Sten S, Podéus H, Sundqvist N, Elinder F, Engström M, Cedersund G. A quantitative model for human neurovascular coupling with translated mechanisms from animals. PLOS Computational Biology. 2023;19(1):e1010818. Available from: https://journals.plos.org/ploscompbiol/article?id=10.1371/journal.pcbi.1010818. doi:10.1371/journal.pcbi.1010818.